

Discovery of Superconductivity and Electron-Phonon Drag in the Non-Centrosymmetric Weyl Semimetal LaRhGe₃

Mohamed Oudah,^{1,*} Hsiang-Hsi Kung,¹ Samikshya Sahu,^{1,2} Niclas Heinsdorf,^{1,2,3} Armin Schulz,³ Kai Philippi,³ Marta-Villa De Toro Sanchez,⁴ Yipeng Cai,⁴ Kenji Kojima,^{1,4} Andreas P. Schnyder,³ Hidenori Takagi,³ Bernhard Keimer,³ Doug A. Bonn,^{1,2} and Alannah M. Hallas^{1,2,5,†}

¹*Stewart Blusson Quantum Matter Institute, University of British Columbia, Vancouver, BC V6T 1Z4, Canada*

²*Department of Physics & Astronomy, University of British Columbia, Vancouver, BC V6T 1Z1, Canada*

³*Max Planck Institute for Solid State Research, Heisenbergstrasse 1, 70569 Stuttgart, Germany*

⁴*TRIUMF, Vancouver, British Columbia, V6T 2A3 Canada*

⁵*Canadian Institute for Advanced Research, Toronto, Ontario, Canada M5G 1M1*

(Dated: May 30, 2024)

We present an exploration of the effect of electron-phonon coupling and broken inversion symmetry on the electronic and thermal properties of the semimetal LaRhGe₃. Our transport measurements reveal evidence for electron-hole compensation at low temperatures, resulting in a large magnetoresistance of 3000% at 1.8 K and 14 T. The carrier concentration is on the order of 10²¹/cm³ with high carrier mobilities of 2000 cm²/Vs. When coupled to our theoretical demonstration of symmetry-protected *almost movable* Weyl nodal lines, we conclude that LaRhGe₃ supports a Weyl semimetallic state. We discover superconductivity in this compound with a T_c of 0.39(1) K and $B_c(0)$ of 2.2(1) mT, with evidence from specific heat and transverse-field muon spin relaxation. We find an exponential dependence in the normal state electrical resistivity below ~ 50 K, while Seebeck coefficient and thermal conductivity measurements each reveal a prominent peak at low temperatures, indicative of strong electron-phonon interactions. To this end, we examine the temperature-dependent Raman spectra of LaRhGe₃ and find that the lifetime of the lowest energy A_1 phonon is dominated by phonon-electron scattering instead of anharmonic decay. We conclude that LaRhGe₃ has strong electron-phonon coupling in the normal state, while the superconductivity emerges from weak electron-phonon coupling. These results open up the investigation of electron-phonon interactions in the normal state of superconducting non-centrosymmetric Weyl semimetals.

I. INTRODUCTION

Semimetals provide a fertile ground for investigating the interplay between topology, superconductivity, and electron-phonon interactions. Starting from the discovery of a Dirac semimetallic state in graphene [1, 2], the study of semimetals has grown to include ever more exotic flavors of topological states in materials with Dirac or Weyl crossings in their band structures [3–5]. Many topological semimetals are simultaneously found to exhibit remarkable transport properties including extremely large and non-saturating magnetoresistances and ultrahigh carrier mobilities [6–8]. In certain semimetals, these transport properties have been definitively linked with strong electron-phonon interactions, including WP₂ [9, 10], PtSn₄ [11, 12], and NbGe₂ [13, 14], all of which also manifest interesting topological states.

One particularly interesting class of semimetals are those with broken inversion symmetry. In metals, broken inversion symmetry leads to electronic and magnetic couplings that are forbidden in centrosymmetric materials, thereby promoting exotic states. One such example is the effect of antisymmetric SOC on superconductivity. ASOC results in the splitting of spin-degenerate bands,

where the energy splitting is proportional to the degree of SOC of the constituent elements. When the ASOC is sufficiently strong, a mixture of spin singlet and spin triplet pairings will occur yielding an unconventional superconducting state [15–19].

The rich physics associated with broken inversion symmetry has led to significant interest in the RTX_3 (R = rare earth, T = transition metal, X = Ge, Si, Sn) family of materials, which crystallize in the non-centrosymmetric $I4mm$ space group. Materials in this family have been known to exhibit heavy fermion behavior, complex magnetic states, and unconventional superconductivity [20–28]. They have also attracted attention in light of their ASOC split Fermi-surfaces [26]. It has been demonstrated in this class of materials that the transition element T plays a crucial role in the splitting of the Fermi-surface, while the R and X elements play a much smaller role [26].

Here, we report a comprehensive characterization of one member of the non-centrosymmetric RTX_3 family, LaRhGe₃, which has significant antisymmetric SOC due to the presence of Rh on the T site. We synthesize single crystals of LaRhGe₃ using a self-flux method for the first time and characterize its low temperature electronic properties via transport, specific heat, muon spin relaxation, and Raman spectroscopy. This ensemble of measurements reveals a rich array of properties in LaRhGe₃ including semimetallicity, superconductivity, and electron-phonon drag. Our electronic structure

* Email: mohamed.oudah@ubc.ca

† Email: alannah.hallas@ubc.ca

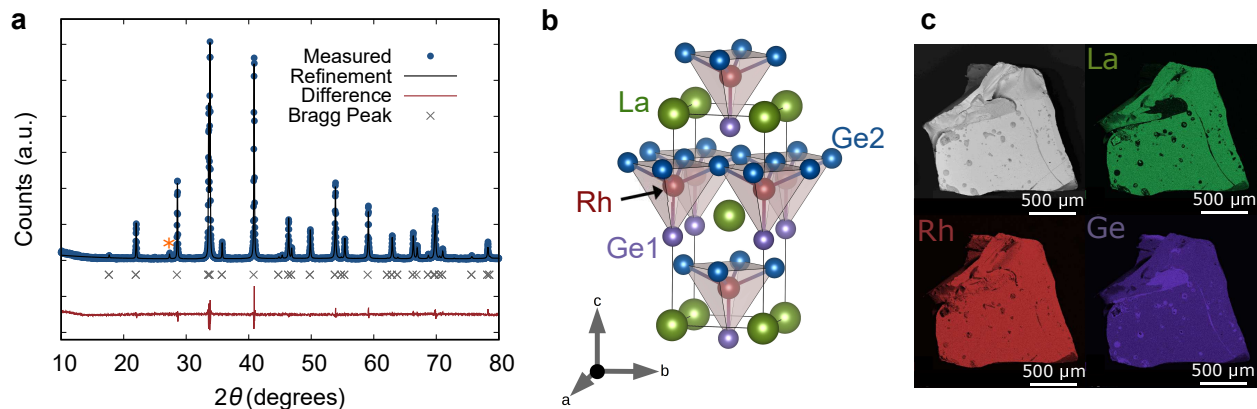


FIG. 1. Structural characterization of LaRhGe_3 . (a) Rietveld refinement of the powder X-ray diffraction pattern of LaRhGe_3 measured at room temperature. The Bragg peak positions for the $I4mm$ space group are indicated by the grey crosses. A small germanium impurity (1.3% by weight) peak is marked with an orange asterisk. (b) The non-centrosymmetric body-centered tetragonal crystal structure of LaRhGe_3 , where La is shown in green, Rh in red, and the two Ge sites are shown in purple and blue, respectively. The broken inversion symmetry is most easily appreciated by considering the positions of Rh within the unit cell. (c) Scanning electron microscopy image of a single crystal of LaRhGe_3 (top left) and elemental mapping on the same crystal for La (top right), Rh (bottom left), and Ge (bottom right). Intensity of colors in the elemental mapping corresponds to the intensity of peaks related to each element, showing uniform distribution of the elements across the crystal.

calculations further reveal topological features of interest, with the discovery of *almost movable* Weyl nodal lines. This set of results on LaRhGe_3 highlights the important role of electron-phonon coupling and paves the way for further exploration of the $I4mm$ class of non-centrosymmetric materials.

II. RESULTS AND DISCUSSION

A. Non-Centrosymmetric Structure of LaRhGe_3

Single crystals of LaRhGe_3 were grown by the metallic self-flux method [29]. To confirm the structural characteristics and crystalline quality of our samples, we performed powder X-ray diffraction (XRD) and energy dispersive X-ray spectroscopy (EDX). The measured powder XRD pattern, given by the blue circles in Fig. 1(a), is consistent with the previously reported body-centered tetragonal $I4mm$ (no. 107) crystal structure [30]. Our Rietveld refinement, shown by the black line in Fig. 1(a), confirms the absence of any significant secondary phases. A minor germanium phase (1.3% by weight based on Rietveld refinement), likely originating from the residual flux on the surface of the crystals, is marked by the orange asterisks. No other impurity phases above the detection limit of our instrument were detected. The fitted lattice parameters for LaRhGe_3 are $a = 4.4187(2)$ Å and $c = 10.0494(5)$ Å. The full results of the Rietveld refinement are presented in Tables S1 and S2.

The spatial homogeneity of our crystals is confirmed by EDX mapping, which shows a uniform distribution of La, Rh and Ge on the sample surface (Fig. 1(c)). A ratio for La:Rh:Ge of 1.00:0.98:2.90 is found based on

EDX analysis, which is close to the expected 1:1:3 ratio. Minor Ge-rich regions can be attributed to residual flux on the crystal's surface, as also detected in the powder XRD measurement.

The non-centrosymmetric crystal structure of LaRhGe_3 is presented in Fig. 1(b). The broken inversion symmetry can be easily discerned by considering the positions of Rh within the unit cell, where Rh sits at the center of the ab -plane with the lower half of the unit cell and at the unit cell edges in the upper half of the unit cell. There are two unique Ge sites in this structure, with the Ge2 site having double the multiplicity of Ge1. The smallest interatomic distances in this structure are between Rh and Ge in a distorted corner-sharing square pyramidal configuration, where the single Rh-Ge1 distance is $2.377(3)$ Å and the four-fold Rh-Ge2 distance is $2.436(7)$ Å. We focus next on the implication of the tetragonal $I4mm$ space group with broken inversion symmetry on the electronic structure of LaRhGe_3 .

B. Electronic Band Structure and Protected Nodal Lines in LaRhGe_3

We calculate the band structure of LaRhGe_3 using density functional theory (DFT). The band structure, which is plotted along the high symmetry directions of the body-centered tetragonal Brillouin zone (Fig. 2), is plotted according to each atomic site (La, Rh, Ge1, and Ge2), where the thickness and intensity of the color represent the weighted atomic contribution. All four atomic sites contribute to the bands closest to the Fermi level. The largest contribution to all the bands that cross the Fermi energy originates from Rh, while Ge1 contributes to the hole bands, and Ge2 contributes to the electron

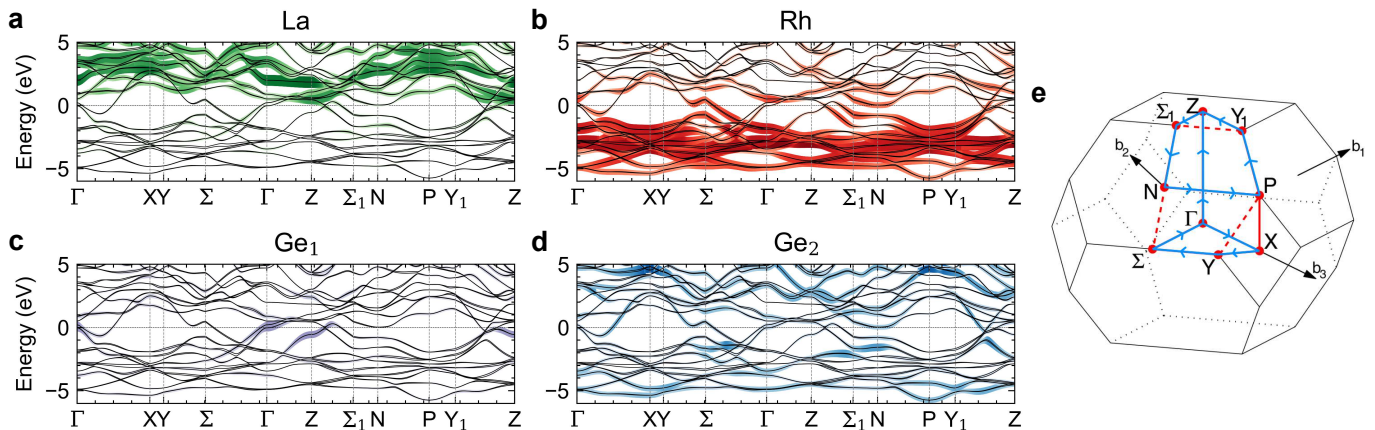


FIG. 2. *Ab-initio* electronic band structures in the primitive unit cell of LaRhGe_3 . The width and intensity of the superimposed colors indicate the contribution to the states from the respective atoms. The dotted horizontal black line marks the Fermi level. An onsite Hubbard interaction of $U_{LDA+U} = 14.5$ eV was added to the f -orbitals of La to push the (unoccupied) states out of the energy window.

bands. Due to the presence of ASOC, the spin degeneracy of all bands is lifted. The ASOC in LaRhGe_3 was thoroughly experimentally characterized as part of a larger study on RTX_3 materials crystallizing in the $I4mm$ space group [26]. The degree of SOC on the transition element T was shown to dictate the degree of splitting of spin-up and spin-down bands, which is enabled by the lack of inversion symmetry in the crystal structure. A significant splitting of the bands is realized in the case of Rh on the T site [26], which is confirmed in our de Haas-van Alphen (dHvA) oscillations, shown in Supplemental Fig. S1. We compare our the splitting in the FFT of the dHvA signal to those previously reported [26] in Table S3, where we find a consistent degree of band splitting in our measurements that confirms a strong ASOC. We will discuss the implications of this strong ASOC on the other observed electronic properties of LaRhGe_3 in the sections ahead.

We next highlight aspects of symmetry-enforced band crossings in LaRhGe_3 . Group theoretical analysis recently predicted *almost movable nodal lines* in a number of tetragonal space groups including the $I4mm$ group to which LaRhGe_3 belongs [31]. Their specific dispersion relation, connectivity, and proximity to the Fermi level are not fully fixed by symmetry alone and are instead found to be material-dependent. In the case of LaRhGe_3 , even though the global Kramers' degeneracy is lifted, the $I4mm$ space group symmetry enforces two types of two-fold degenerate nodal lines throughout the Brillouin zone. Consider the mirror plane that intersects the rotational axis ($\Gamma - Z$) and the N -point. The eigenvalues of the mirror symmetry at N are $\pm i$. Because N is a time-reversal invariant momentum (TRIM) point, the $+i$ and $-i$ eigenvalues are paired, enforcing a two-fold degeneracy at this point. Let \mathbf{k}_1 and \mathbf{k}_2 be two k -points on the mirror plane that are related by time reversal. Because they are time reversal partners, their mirror eigenvalues have opposite

phases. Therefore, along an arbitrary path on the mirror plane that connects \mathbf{k}_1 and \mathbf{k}_2 (which does not cross a TRIM point), the eigenvalues must be exchanged. Since this can only happen at band crossings and we have the freedom to choose any path, the intersections must form a nodal line that connects the N -points. That type of degeneracy is called an *almost movable* nodal line [31]. It is only pinned at the two TRIMs that it connects and, in contrast to a point-like topological band feature (*e.g.* a Weyl point), it is extended in both k -space and energy. The same argument holds for the Γ - and Z -point. However, the presence of additional symmetry pins the nodal line to the rotational axis. Hence, there are two ways the almost movable nodal line can connect the N -points: It either intersects the pinned nodal line ($\Gamma - Z$) or it does not.

In Figure 3(a) and 3(b) the two types of connectivity are shown. The intensity of the heatmap corresponds to a quantity similar to a spectral function that has poles at k -points where a chosen pair of bands becomes degenerate. The overlay shows the body-centered primitive Brillouin zone (type 2) and the high-symmetry points that lie within the plane spanned by $\Gamma - Z$ and $\Gamma - N$. The almost movable nodal lines connect the N -points on (seemingly arbitrary) paths that depend on the specific dispersion relation of the chosen pair of bands. Thus, the evolution of the almost movable nodal lines through k -space for different band pairs varies drastically.

Figure 3(c) shows the dispersion relation along the different nodal lines. The pinned and the almost movable nodal lines shown in Fig. 3(a) are close to the Fermi energy and can potentially be tuned to the Fermi edge by either doping or applying a gate voltage. Due to the dispersive nature of the nodal lines, there is a large energy region in which the degeneracies can be accessed in contrast to point-like topological band crossing, and thus a wider range of parameters in which drumhead surface

states can be found [32, 33]. Even though surface states do not necessarily emerge in nodal line systems [34], any curve through k -space that encircles a single nodal line has a Berry curvature that is quantized to π by the mirror symmetry. A suitable surface termination can likely be found for which gapless surface states appear at k -points of the two-dimensional surface Brillouin zone that connect projections of the different nodal lines in the bulk.

Materials with these gapless and robust surface modes are highly sought-after, due to the variety of proposals in novel device applications [3, 35–41]. In realistic materials, disorder and defects weakly break the crystal symmetries that protect both the nodal lines and their edge modes. However, as long as the symmetries are approximate and the effect of the perturbation is small compared to the topological gap, the edge modes remain present [42, 43]. Interaction effects might also weakly break symmetries, but more importantly they generically obstruct an exact description of a material’s electronic structure using single-particle states, which the definition of most topological invariants relies on. Nevertheless, it has been shown that an interacting system can always be adiabatically connected to a noninteracting system with the same topology, as long as the interaction does not drive a phase transition [44–47]. Even nonlinear perturbations do not generically suppress edge modes [48], and their stability in nodal line semimetals in their superconducting state has been theoretically demonstrated [49]. Therefore, realizing superconducting state, even a conventional one mediated by electron-phonon coupling, in the bulk of a nodal line semimetal can allow for exotic pairing on the surface due to interaction with the topological surface state.

C. Semimetallicity in LaRhGe₃

We next highlight the semimetallic nature of LaRhGe₃ experimentally, which, along with our nodal-line predictions, demonstrate that it is a Weyl semimetal. Electrical transport measurements confirm the metallic nature of this material, with a longitudinal resistivity that monotonically decreases with decreasing temperature and resistivity magnitudes in the $\mu\Omega$ -cm range across all temperatures (Fig. 4(a)). The high residual resistivity ratio, $\rho_{300\text{K}}/\rho_{2\text{K}} = 110$, is suggestive of the good crystalline quality of our samples. As a function of increasing applied magnetic field, there is a rapid increase in the low temperature resistivity, below 50 K. For fields larger than 6 T, the resistivity reaches a minimum value before a low temperature upturn and then ultimately plateaus for temperatures below 10 K. In Fig. 4(b), we plot the magnetoresistance (MR) of LaRhGe₃ at various temperatures, where MR is defined as $[\rho_{xx}(B) - \rho_{xx}(0)]/\rho_{xx}(0)$. The MR remains unsaturated in fields up to 14 T, where it reaches a value of 30 at 1.8 K. The large and unsaturated MR and the field-driven resistivity upturn in LaRhGe₃ are characteristic of a compensated

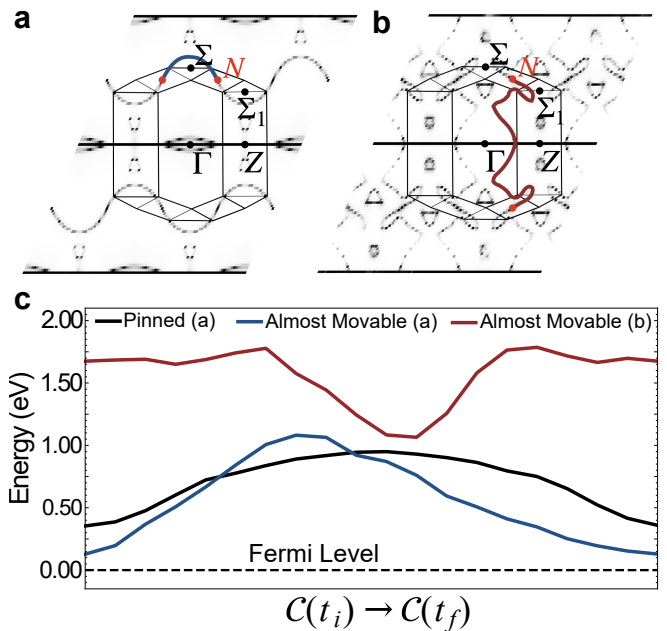


FIG. 3. Almost movable nodal lines in LaRhGe₃. (a,b) Pinned (Γ to Z , black) and almost movable nodal lines (N to N , (a) blue and (b) red) in the mirror plane of the Brillouin zone of the type 2 body centered tetragonal primitive unit cell. The projection of the Brillouin zone onto this mirror plane, as well as the high-symmetry points that lie therein are given in the overlay. The connectivity of almost movable nodal lines is not completely determined by the space group symmetry. The two possibilities are both realized in the material for different pairs of bands. (a) The almost movable nodal line connecting two N -points. (b) Same as (a), but intersecting the pinned nodal line. (c) The dispersion along curves C through k -space along the pinned nodal line from (a) (black), the almost movable nodal line from (a) (blue), and the almost movable nodal line from (b) (red). t parameterizes the curve with $C(t_i)$ and $C(t_f)$ being the initial and final point of the curves respectively. The pinned and the almost movable lines from (a) are close to the Fermi level.

semimetal [51–53]. We perform a scaling analysis of the MR over the various temperatures measured, as shown in the supplemental materials Fig. S2, and find good agreement with Kohler’s rule.

To verify the semimetallicity scenario, we measured the Hall resistivity ρ_{xy} of LaRhGe₃, shown in Fig. 4(c), at the same fields and temperatures as the MR. We find that $\rho_{xy}(B)$ is non-linear for all temperatures, and hence it cannot be fitted with a semi-classical one-band model for which ρ_{xx} would be independent of field, also in disagreement with our data. This is expected if we examine the band structure of LaRhGe₃, shown in Fig. 2, where we find three pairs of spin-split bands crossing the Fermi level, where two pairs are hole bands and one pair is an electron band. While the electron Fermi surfaces are larger than the hole Fermi surfaces, we fitted both the MR and Hall resistivity to a semi-classical two-band model [50] that assumes density and mobility of all hole

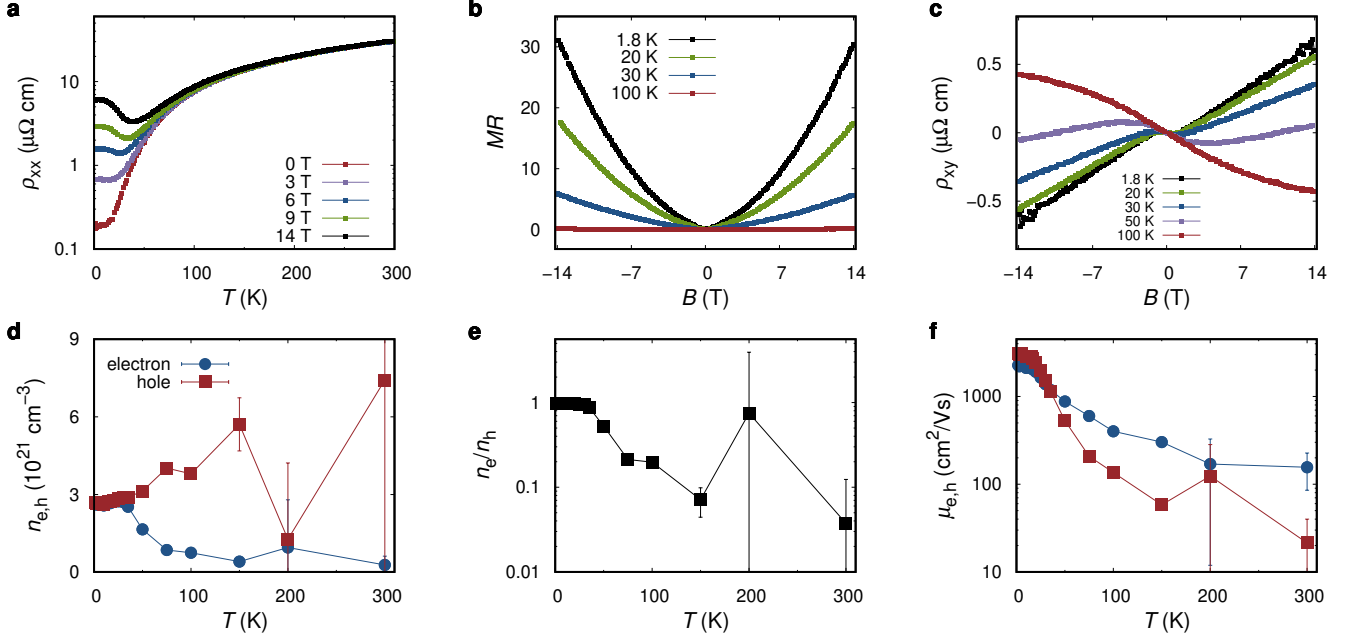


FIG. 4. Semimetallic electronic properties of LaRhGe₃. (a) Temperature dependence of the longitudinal resistivity ρ_{xx} measured in different magnetic fields, showing sizable magnetoresistance below 50 K. (b) Magnetic field dependence of the magnetoresistance (MR) as defined in text measured at various temperatures, reaching a value of 30 by 14 T at 1.8 K. (c) Hall resistivity ρ_{xy} measured at various temperatures, showing a change of sign upon cooling below 50 K. (d) Electron and hole carrier densities, (e) their ratio, and (f) carrier mobilities extracted from fits of MR and ρ_{xy} to a two-band model [50], revealing LaRhGe₃ to be a compensated semimetal at low temperatures.

and electron carriers can each be captured with a single term:

$$\rho_{xx} = \frac{1}{e} \frac{(n_h \mu_h + n_e \mu_e) + (n_h \mu_e + n_e \mu_h) \mu_h \mu_e B^2}{(n_h \mu_h + n_e \mu_e)^2 + (n_h - n_e)^2 \mu_h^2 \mu_e^2 B^2} \quad (1)$$

$$\rho_{xy} = \frac{B}{e} \frac{n_h \mu_h^2 - n_e \mu_e^2 + (n_h - n_e) \mu_h^2 \mu_e^2 B^2}{(n_h \mu_h + n_e \mu_e)^2 + (n_h - n_e)^2 \mu_h^2 \mu_e^2 B^2}. \quad (2)$$

The fitting parameters in this model are the carrier densities, n_e and n_h , and the carrier mobilities, μ_e and μ_h , for electrons and holes, respectively. We simultaneously fit ρ_{xx} and ρ_{xy} to this two-band model to extract $n_{e,h}$ and $\mu_{e,h}$ as a function of temperature. The carrier densities, plotted in Fig. 4(d), are on the order of 10^{21} cm^{-3} , a high carrier density semimetal, such as HfB₂ [54] and LaAlGe [55] with similar carrier densities.

At high temperatures, we find that holes are the majority charge carriers but when the temperature falls below 40 K, the carrier densities are essentially compensated with $n_e/n_h = 0.99(1)$ at 2 K, as can be seen in Fig. 4(e). For both holes and electrons, the mobility increases with decreasing temperature, as can be expected due to reduced scattering of charge carriers by phonons. At high temperature the electron mobility is larger than the hole mobility, as can be seen in Fig. 4(f). We should note, however, that the error bars in this fitting range

are large due to the small magnetoresistance above 100 K and the limitations of the two band model. Upon cooling, the hole mobility increases more rapidly and exceeds the electron mobility for temperatures where the carriers are compensated, below 40 K, explaining the sign change observed in ρ_{xy} in the same temperature range. The high hole mobility of $0.3 \text{ m}^2/\text{Vs}$ at low temperature again demonstrates the good crystal quality, which is also relevant to the non-saturating MR of LaRhGe₃ and the electron-phonon interactions discussed in Sec. III E. We have experimentally verified the semimetallic nature of LaRhGe₃, and in the next section demonstrate the discovery of superconductivity in this Weyl semimetal.

D. Superconductivity in LaRhGe₃

Our first indication of superconductivity in LaRhGe₃ comes from low temperature specific heat measurements. We observe a sharp lambda-like anomaly at $T_c = 0.39(1) \text{ K}$ as can be seen in the electronic part of the specific heat C_{el} , as shown in Figure 5(a), where the lattice contribution has been subtracted by fitting the zero-field data above the transition. Upon application of small magnetic fields, the transition is suppressed to lower temperatures. We find that the transition remains sharp for applied fields of 0.5 mT and 1 mT, despite the decrease in T_c , which is consistent with the first order field-induced

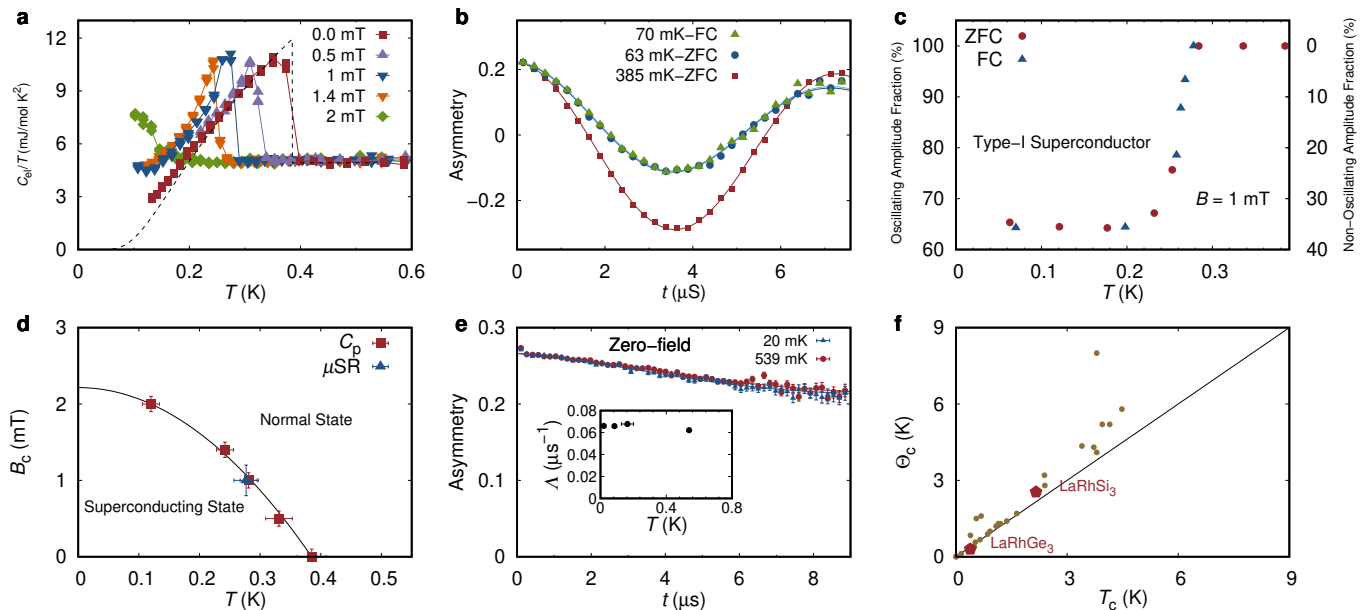


FIG. 5. Superconducting transition in LaRhGe₃. (a) Temperature dependence of C_{e1}/T measured in varying magnetic fields. The superconducting transition seen at 0.39(1) K in 0 mT is suppressed with increasing magnetic field. (b) Representative transverse field muon decay asymmetry spectra collected above and below T_c in LaRhGe₃ under an applied magnetic field of 1.0 mT. (c) The oscillating and non-oscillating amplitude of the signal in (b) as a function of temperature measured in zero-field cooling (ZFC) and field cooling (FC) protocol. Reduction in the oscillating amplitude is due to expulsion of magnetic field in the superconducting state, and the ZFC and FC show similar suppression, demonstrating type-I superconductivity. (d) Plot of Θ_c against measured T_c for various elemental type-I superconductors, LaRhSi₃, and LaRhGe₃. LaRhGe₃ falls on the black solid line, which represents the expectation based on weak-coupling BCS theory. (e) Field dependence of the T_c values extracted from C_P and transverse field μ SR. The solid line is a fit to the expression, Eq. 7, in the text to estimate $B_c(0) = 2.2$ mT. (f) Zero field μ SR spectra collected at 539 mK and 20 mK, with fit using Kubo-Toyabe function for the data. No significant change is seen between the data above and below T_c . Inset shows the resulting relaxation rate σ .

suppression of superconductivity expected for a type-I superconductor [56–58] and comparable to what has previously been observed in LaRhSi₃ [59]. Upon application of a 2 mT field, the superconducting transition is fully suppressed in our measurement window, which extends down to 0.1 K. The magnitude of the specific heat jump, $\Delta C/C_{en} \sim 1.43$, as shown in shown in Fig. S3(a), is consistent with a BCS model in the weak-coupling limit. C_P data before subtraction of the phonon part are shown in Fig. S4. Further analysis of this specific heat data, as described in the Supplemental Materials, allows a number of superconducting parameters to be derived, and these are presented in Table I.

We next present muon spin relaxation and rotation (μ SR) measurements on LaRhGe₃. Muons are highly sensitive to their local magnetic environment, making them an excellent probe of field expulsion in superconductors and spontaneous time-reversal symmetry breaking. We begin by investigating the former, where the muon decay asymmetry plotted as a function of time in an applied field of 1 mT (which is below the critical field) is shown in Fig. 5(b). In this geometry, the direction of the magnetic field is transverse to the muon spin. Above the superconducting transition, at 385 mK, the muons that land in the sample or the sample holder will couple

to the applied field and undergo Larmor precession, yielding an oscillatory decay asymmetry. Whereas, within the superconducting state at 70 mK, the magnetic field is expelled and the muons that land in the sample will not precess, giving rise to a flat decay asymmetry. The remnant oscillatory signal originates from the fraction of muons that land outside the superconducting sample. We fit the asymmetry spectra using a two-term asymmetry function

$$G_{TF}(t) = A \left[f \exp(-\lambda t) \cos(\omega_1 t + \phi) + (1 - f) \exp\left(\frac{-\sigma^2 t^2}{2}\right) \right] \quad (3)$$

where the first term captures the signal from muons stopping in the silver sample holder and non-superconducting part of the sample and the second term captures the signal from muons stopping in the superconducting part of the sample. The fraction of signal from muons that land in silver sample holder and non-superconducting part of the sample is given by f , and ω_1 is the muon precession frequencies in the background. The A term is the total asymmetry and the ϕ is the initial phase of the muons. The depolarization rates for the sample and the background signals, respectively, are given by σ and λ . A global fit was used for all variables, but the fraction f

was allowed to be refined with temperature. The value of f as a function of temperature under both ZFC and FC conditions is shown in Fig. 5(c). The 100% oscillating amplitude corresponds to all muons stopping inside LaRhGe₃ above T_c and the non-superconducting silver plate. A sharp drop in the oscillating amplitude is observed at the superconducting transition. This behavior is expected in a superconductor due to the expulsion of the magnetic field from the bulk of the sample in the superconducting state such that muons implanted sufficiently deeply in the sample will not be affected by the applied field and will therefore not precess. We estimate about 40% of the signal amplitude corresponds to the sample based on the sample coverage, so the drop to about 60% corresponds to the expulsion of the field from most of the sample. We show a shift in the amplitude from the oscillating component to the zero-field in Fig. S5. From these transverse field μ SR measurements, we estimate $T_c \sim 0.28$ K in an applied field of 1 mT, in good agreement with the T_c measured in specific heat at 1 mT. We find that the suppression of the amplitude is approximately equivalent under ZFC and FC conditions at the lowest temperatures, which further supports the conclusion that LaRhGe₃ is a Type-I superconductor.

TABLE I. Superconducting parameters of LaRhGe₃.

Parameter	Value	Units
T_c	0.39(1)	K
$B_c(0)$	2.2(1)	mT
γ_n	4.92(4)	mJ mol ⁻¹ K ⁻²
β	0.25(1)	mJ mol ⁻¹ K ⁻⁴
θ_D	341(10)	K
λ_{ep}	0.34(2)	-

The temperature and field dependence of T_c extracted from specific heat and transverse field μ SR are plotted in Fig. 5(d). We estimate the zero-temperature critical field $B_c(0)$ using the conventional relationship, $B_c(T) = B_c(0) \left[1 - (T/T_c)^2\right]$, where T_c is 0.39(1) K. This fit yields the curve shown by the black line and a $B_c(0)$ of 2.2 mT. The small critical field value makes the presence of a remnant magnetic field during the C_P measurement a serious concern that can shift our measured T_c . However, to address this concern we highlight the good agreement with the point on this phase diagram extracted from transverse field μ SR measurement, shown in blue. This point is expected to be accurate due to the high-resolution field-zeroing protocol employed in that experiment.

Our attempts to measure the electric resistivity of LaRhGe₃ in a dilution refrigerator reveal a drop in the resistivity at a temperature that is commensurate with the onset of superconductivity, as shown in Fig. S4(b). This resistance drop is partially suppressed by an applied magnetic field of 1.0 mT. However, even in the zero field

measurement, we detect a finite resistance in the superconducting state, which we ascribe to the applied current exceeding the critical current threshold of LaRhGe₃. The low critical current suggested by our resistivity measurements is not particularly surprising given the extremely low critical field of 2.2 mT.

Finally, we performed zero field μ SR measurements to look for any sign of spontaneous magnetic fields and time-reversal symmetry breaking as LaRhGe₃ enters its superconducting state. The magnetic field at the sample position was carefully zeroed following the protocol described in the methods. High statistics zero field spectra were collected above and below T_c with representative spectra shown in Fig. 5(e). In the absence of magnetism, the muon depolarization is due to randomly oriented nuclear moments and can be described by the Kubo-Toyabe function

$$G_{\text{KT}}(t) = \frac{1}{3} + \frac{2}{3} (1 - \sigma^2 t^2) \exp\left(-\frac{\sigma^2 t^2}{2}\right)$$

where σ accounts for the field generated by the randomly nuclear moments at the muon site. The relaxation spectra for LaRhGe₃ is fitted to the function

$$A(t) = A_S G_{\text{KT}}(t) \exp(-\Lambda t) + A_{BG}$$

where A_S and A_{BG} represent the sample and background asymmetry, respectively, while Λ accounts for any additional relaxation rate. Our fits reveal no significant change in Λ above and below T_c , as shown in the inset of Fig. 5(e), confirming the absence of any significant TRS breaking in LaRhGe₃.

Type-I superconductivity is common among pure elements but relatively rare in compounds, particularly beyond binaries. LaRhGe₃ is therefore one of very few [59–62] type-I superconductors containing more than two elements. In Fig. 5(f), we compare the calculated critical temperature, denoted as θ_c , based on the γ_n and $B_c(0)$ values [63], with the measured T_c for various elemental type-I superconductors, LaRhSi₃ [59], and LaRhGe₃. We find that LaRhGe₃, as well as LaRhSi₃, lie close to the solid-black line that represents the expectation based on weak-coupling BCS, further confirming that LaRhGe₃ is a type-I superconductor in the weak-coupling limit. Nevertheless, we expect topologically protected states on the surface of LaRhGe₃, as described in Section II B may allow for novel pairing on the surface despite the conventional nature of the bulk. Next we highlight electron-phonon interactions in the normal state of LaRhGe₃, which, unlike the superconducting state, hint at strong coupling.

E. Electron-Phonon Drag in LaRhGe₃

Finally, we return to the normal state of LaRhGe₃ to investigate the thermal properties of this material. Our first indication of unusual transport behavior comes

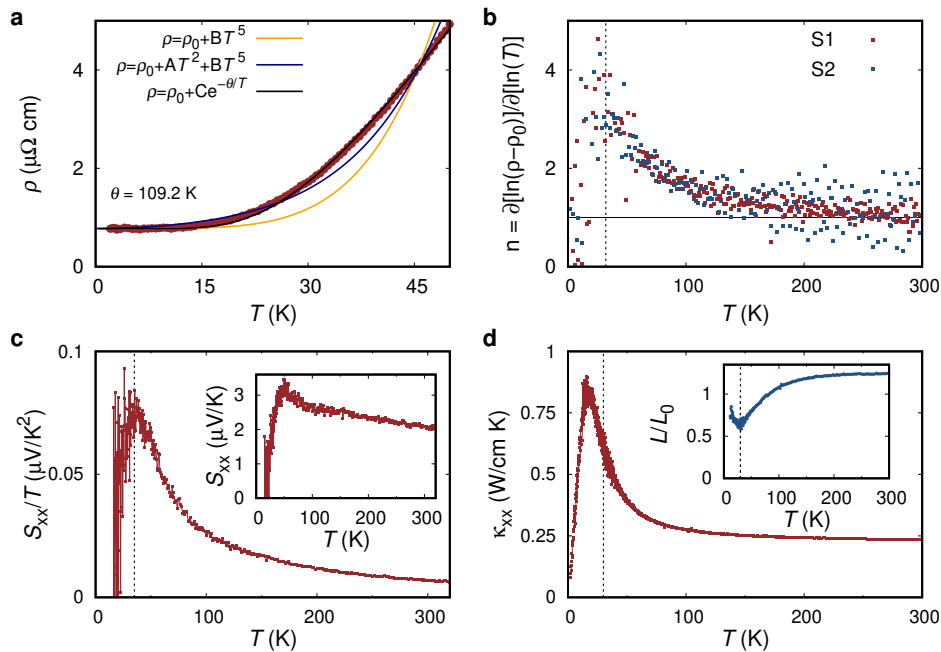


FIG. 6. Phonon drag in LaRhGe₃ detected by transport measurements. (a) Resistivity as a function of temperature measured along *ab*-plane of LaRhGe₃ in zero-field, and different models fitted to the data below 50 K. (b) n , the exponent of the temperature dependent resistivity determined derivative of $\ln(\rho - \rho_0)$ vs. $\ln(T)$ as a function of temperature. Data for two samples, S1 and S2, are shown. (c) Temperature dependence of Seebeck coefficient over temperature (S_{xx}/T) as a function of temperature of LaRhGe₃. Inset shows S_{xx} as a function of temperature. (d) Temperature dependence of thermal conductivity of LaRhGe₃. Inset shows the Lorenz number as a function of temperature. The dashed vertical line in panels (b,c,d) marks the approximate phonon drag temperature.

from zero-field resistivity where we observe a deviation from a standard Fermi liquid behavior as shown in Fig. 6(a). Even using a modified Bloch-Grüneisen model $\rho = \rho_0 + AT^2 + BT^5$, where the T^5 term accounts for electron-phonon interactions and the additional T^2 term accounts for electron-electron interactions, a poor fit is obtained below 50 K. Instead, we find that the resistivity data are better described by the exponential form of a phonon-drag model, $\rho = \rho_0 + Ce^{-T_0/T}$ [13, 64], where the activation temperature is $T_0 = 110$ K. We find an equally good agreement with the data using a power law fit $\rho = \rho_0 + CT^n$, which yields $n = 2.9$, as shown in Sup. Fig. S6. To further analyze the temperature dependence of the resistivity we take the logarithmic derivative after subtracting residual resistivity to quantify the exponent $n = [\delta \ln(\rho - \rho_0)]/[\delta \ln T]$. The temperature dependence of n is presented in Fig. 6(b) for two different samples, and we find at high temperature $n \sim 1$ as expected in a standard Bloch-Grüneisen picture. However, we find an upturn towards $n \sim 3$ at low temperatures, which is consistent with $n = 2.9$ from our power law fit.

Further evidence for the phonon-drag scenario comes from Seebeck coefficient measurements, shown in the inset of Fig. 6(c), where we notice a maximum at around ~ 50 K signaling the interaction between phonons and electrons is enhanced at low temperature. When scaled by temperature, S_{xx}/T , plotted in the main panel of

Fig. 6(c), the peak appears at a temperature of ~ 30 K similar to the peak in the derivative of the resistivity. Coincident with these two features, a peak also appears below 50 K in the thermal conductivity, shown in Fig. 6(d). Typically, the Lorenz number is evaluated by dividing the electronic part of the thermal conductivity by the electrical conductivity, but separating the phonon and electron parts of the thermal conductivity proved difficult with our current data. Instead, we show the total thermal conductivity divided by electrical conductivity, representing an upper limit of the Lorenz number, in the inset of Fig. 6(d), which shows clear deviation at low temperature with a minimum around 30 K. It's worth noting that no clear deviations in the scaling behavior of the MR is detected at this temperature, as shown in Fig. S2.

The peaks in κ_{xx} , S_{xx}/T , and the resistivity derivative all appear close to ~ 30 K, which we take as the phonon-drag temperature. Comparing this with the Debye temperature or 340 K, we find $\Theta_{\text{ph-drag}}/\Theta_D \sim 10$, which has been seen in other materials with phonon-drag [1]. In Sec. II C, we noted that the MR is significantly enhanced below 30 K due to electron-hole compensation. At the same temperature, we also observed a crossover of the carrier mobilities with the holes having higher mobilities in the low-temperature limit and both electron and hole mobilities plateauing in this temperature range. There-

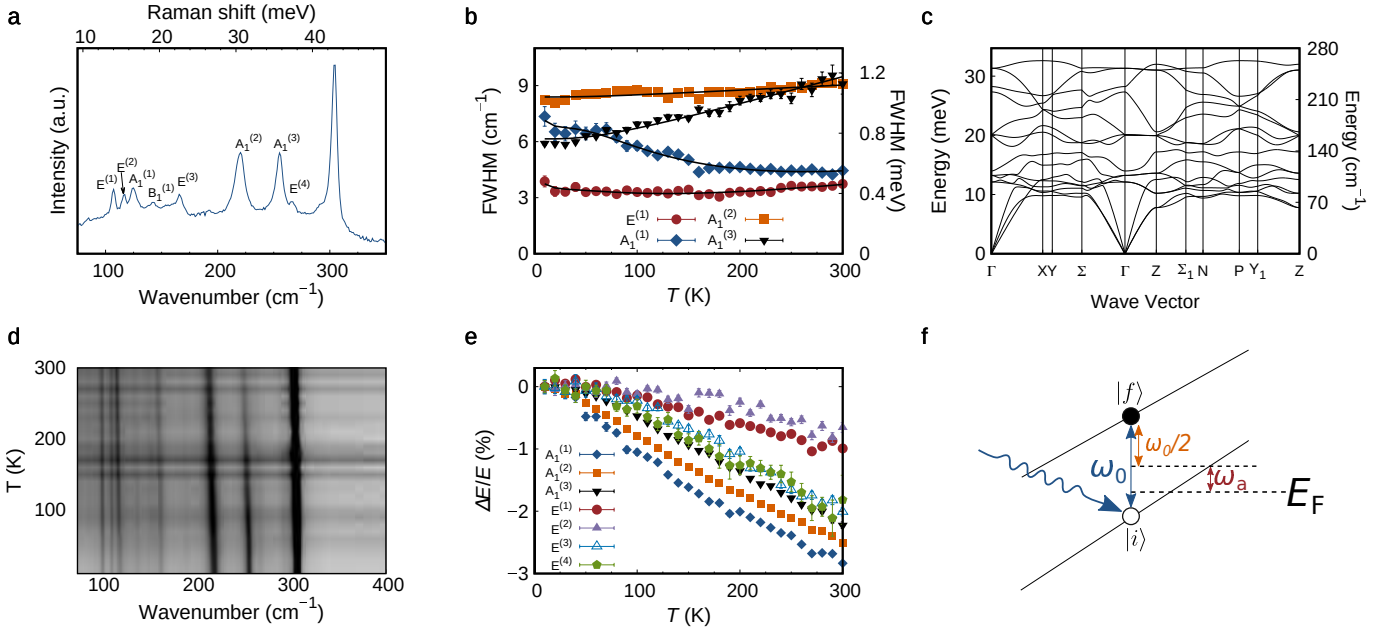


FIG. 7. Electron-phonon drag in LaRhGe₃ detected by Raman spectroscopy. (a) Raman spectra of LaRhGe₃ measured at 10 K. The phonon mode symmetries are labelled in accordance with our DFT calculations. The strong peak at 300 cm⁻¹ is due to Ge flux on the surface. (b) Black and white map of Raman scattering intensity plotted as a function of temperature and Raman shift measured from the (101) surface of LaRhGe₃ crystal. (c) Full width at half maximum (FWHM) temperature dependence of $A_1^{(1)}$, $A_1^{(2)}$, $A_1^{(3)}$, and $E^{(1)}$ modes based on fits described in the text. Solid black lines correspond to fits to the temperature dependence of each phonon mode based on Eq. 4. (d) Percent difference of the phonon energies of A_1 and E modes from energies at 10 K as a function of temperature. (e) Calculated phonon dispersion curves along high-symmetry lines of the tetragonal primitive unit cell of LaRhGe₃. Anomalous temperature dependence of the $A_1^{(1)}$ phonon lifetime in LaRhGe₃. (f) Schematic depicting excitation of electron-hole pairs by optical phonons, where ω_a is the energy offset to take into account that the Fermi level is not exactly halfway between the initial state $|i\rangle$ and final state $|f\rangle$ and ω_0 is the bare phonon energy.

fore, the low-temperature increase in κ_{xx} and S_{xx}/T can be attributed to and electron-phonon interactions dominating over phonon-phonon interactions.

To confirm this scenario, we measured the Raman spectra of LaRhGe₃ to search for signatures of phonon linewidth broadening due to electron-phonon coupling. Due to the lack of inversion symmetry, all 12 optical phonons in LaRhGe₃ are Raman active, which we will denote by the irreducible representations of the C_{4v} point group to 8 optical phonons, where 4 of them are doubly degenerate: $3A_1 + B_1 + 4E$ [65]. Using the Raman selection rules and polarization optics [66], we identify the symmetry of each peaks at 121, 214, and 249 cm⁻¹ as the three A_1 phonons, the peak at 139 cm⁻¹ is a B_1 phonon, whereas the peaks at 106, 116, 163, and 262 cm⁻¹ are the phonons with E symmetry (Fig. S7). The Raman spectrum measured at 10 K without any analyzing polarizer is shown in Fig. 7(a) with all phonon modes labeled. We tabulate the measured phonon energies alongside the values calculated from DFT in Table S5 to justify our mode assignment. We also notice that there are two unaccounted peaks at 153 and 189 cm⁻¹, which we designate as phonon overtones, *i.e.* the simultaneous excitation of two phonons carrying opposite momenta. Our assignment is justified by the DFT calculated phonon

(Fig. 7(e)), where the acoustic phonon branch has maximum energy around 80-90 cm⁻¹.

The Raman spectra were measured between 10 and 300 K in 10 K intervals as shown in Fig. 7(b) and Fig. S8. In order to maximize the signal-to-noise ratio and track all phonon modes simultaneously, the temperature-dependent measurements were done without the analyzing polarizer. The phonon energies and full-width at half maxima (FWHM) were extracted by fitting to Lorentzian line shapes, as shown in Fig. S9 for spectra collected at 10 K and 300 K. The resulting temperature dependence of the FWHM and energy of select phonon modes are presented in Fig. 7(c) and (d), respectively. At a qualitative level, we note that the energy shifts show a conventional shift to lower energies with increasing temperature for all modes. Meanwhile, a more complex behavior is uncovered for the FWHM, with some modes showing an unexpected narrowing with increasing temperature.

In most materials, the phonons acquire finite linewidths through three channels: impurity scattering (γ_0), anharmonic phonon-phonon interaction ($\gamma_{3p}(T)$), and electron-phonon coupling ($\gamma_{ep}(T)$) [67, 68]:

$$\gamma(T) = \gamma_0 + \gamma_{3p}[1 + n(\omega_1, T) + n(\omega_0 - \omega_1, T)] + \gamma_{ep}[f(\omega_a - \omega_0/2) - f(\omega_a + \omega_0/2)]. \quad (4)$$

The temperature dependence of the FWHM is typically dominated by the anharmonic “three-phonon process” given by the second term in Eq. 4. Here, a $q = 0$ optical phonon of ω_0 decays into two phonons with opposite momenta and energies ω_1 and $\omega_0 - \omega_1$, and $n(\omega, T)$ is the Bose distribution function. The last term in Eq. 4 accounts for the line width due to the excitation of an electron from state (k, i) to (k, j) by absorbing an optical phonon of energy ω_0 (Fig. 7(f)), where $f(\omega, T)$ is the Fermi distribution function. The constant γ_{ep} is directly related to the electron-phonon coupling constant, $\lambda = \frac{4}{\pi N(0)} \sum_j \gamma_{ep,j} / \omega_{0,j}^2$ with $N(0)$ being the density of states at the Fermi energy [68]. The asymmetric coefficient, ω_a is a phenomenological fitting parameter accounting for the fact that the Fermi level may not lie exactly halfway between the electron and hole states, as shown in Fig. 7(f). The electron-phonon induced linewidth is typically negligibly small compared to the anharmonic contribution. This is because $q = 0$ phonons generally only promote vertical interband transitions to conserve both energy and momentum, and therefore have very limited phase space to excite electron-hole pairs.

We have fitted the temperature dependence of each phonon mode in LaRhGe₃ to Eq. 4 and the results are tabulated in Table S5. The three highest energy phonons (including $A_1^{(2)}$ and $A_1^{(3)}$ in Fig. 7(c)) exhibit a conventional temperature dependence and are well captured by impurity scattering and anharmonic processes alone. However, we find that the FWHM of the five lowest energy phonons deviates from the prediction of the anharmonic decay model, and could only be well described by adding the electron-phonon interaction term. The most extreme disagreement occurs for the $A_1^{(1)}$ phonon whose width increases markedly with decreasing temperature (Fig. 7(c)). Similar effects have been observed in graphite and graphene [67, 69], and more recently in WP₂ and NbGe₂ as a signature of the phonon drag effect [10, 13]. Among the phonon modes of LaRhGe₃, the $A_1^{(1)}$ phonon also shows the greatest relative change in energy as a function of temperature, as can be seen in Fig. 7(d).

Unlike the line width, electron-phonon coupling has little effect on the phonon energy where the temperature dependence is contributed by two major factors: lattice thermal expansion and anharmonic phonon-phonon interaction [70]:

$$\omega(T) = \omega_0 e^{-3\gamma_G \alpha_0 T} - \omega_{3p} [1 + n(\omega_1, T) + n(\omega_0 - \omega_1, T)]. \quad (5)$$

The first term accounts for the lattice thermal expansion, where ω_0 is the bare phonon energy, γ_G is the mode Grüneisen parameter, and α_0 is the temperature independent linear thermal expansion coefficient. The second term arises from the same three-phonon anharmonic decay process as in Eq. 4. We show the change in relative energy of the A_1 and E modes in Fig. 7(d) and all of the fitting parameters are tabulated in Table S5. All phonon energies decrease monotonically with increasing temperature, indicating they are dominated by

the three-phonon anharmonic term in Eq. 5. In some materials, it is necessary to include higher-order anharmonic terms to describe the temperature dependence of phonon self-energy [67, 71]. In LaRhGe₃, we find it only marginally improves the fit for the phonon energies and has little effect on the line width. This gives us confidence that the observed anomalous temperature dependence of the phonon linewidths cannot be caused by higher order anharmonic terms, and is more likely a signature of electron-phonon drag.

III. SUMMARY

Our study establishes LaRhGe₃ as a remarkable material with many intertwined novel electronic properties. Our transport measurements demonstrate that LaRhGe₃ is a compensated semimetal while our electronic structure calculations reveal Weyl nodal-line states due to the $I4mm$ space group. We report the discovery of superconductivity in LaRhGe₃ with a T_c of 0.39(1) K and a $B_c(0)$ of 2.2(1) mT. We find that LaRhGe₃ is a type-I superconductor and well described by weak-coupling BCS theory with no evidence for TRS breaking in the zero field μ SR measurement suggesting a dominant singlet pairing in the measured temperature range, despite the strong antisymmetric SOC.

In the normal state, we find that the temperature dependence of resistivity in zero-field deviates from that of a typical Fermi liquid. We identify a peak in the derivative of the resistivity, the Seebeck coefficient, and in thermal conductivity at ~ 30 K, which is consistent with phonon drag in LaRhGe₃. We measure the temperature-dependent Raman spectra of LaRhGe₃ and find anomalous temperature dependence of phonon line widths that can be explained by assuming electron-phonon coupling. This appears prominent in the temperature dependence of the FWHM of the lowest energy A_1 mode.

With the rich literature on superconductivity in materials crystallizing in the RTX_3 structure, we draw some comparisons with LaRhGe₃ and find it similar to the previously reported LaRhSi₃. However, our current work indicating semimetallicity and electron-phonon drag in the normal state highlights a new area of interest in the class of non-centrosymmetric materials crystallizing in the $I4mm$ space group. More work is needed to clarify the pairing state in the superconducting phase of LaRhGe₃. Furthermore, the theoretically predicted *almost movable* nodal line will push further investigation of topology, both theoretically and experimentally, in the RTX_3 family of materials.

IV. METHODS

A. Synthesis and Structural Characterization

Single crystals of LaRhGe₃ were grown from Rh-Ge self flux. The elements La, Rh, and Ge in the molar ratio 1:2:7 were loaded into an Al₂O₃ Canfield crucible set and sealed in a quartz tube under 0.3 atm argon pressure. The mixture was then slowly heated to 1200 °C and held at this temperature for 6 h followed by cooling to 975 °C over 60 h. At 975 °C, the crystals were separated from the flux by centrifuging at 2000 rpm for approximately 30 s. The as-grown crystals were shiny with dimensions up to $3 \times 2 \times 1$ mm³, and are stable in air on a time scale of weeks but develop surface oxidation over more extended periods of air exposure. Phase purity and orientation of the crystals were confirmed by X-ray diffraction (XRD) using a Bruker D8 Advance with Cu K α_1 radiation ($\lambda = 1.54056$ Å). The composition and homogeneity were confirmed through energy dispersive X-ray spectroscopy (EDX) using a Philips XL30 scanning electron microscope equipped with a Bruker Quantax 200 energy-dispersion X-ray microanalysis system and an XFlash 6010 SDD detector.

B. Transport and Specific Heat

Electrical resistivity measurements were performed with conventional four- and five-probe geometries using a Quantum Design Physical Property Measurement System (PPMS). For these measurements Pt wires (25 μ m) were attached to the sample with silver epoxy. Specific heat measurements were performed using a PPMS with a ³He/⁴He dilution refrigerator insert. Thermal conductivity and Seebeck measurement were performed using a thermal transport option for the PPMS.

C. μ SR Measurements

Muon spin relaxation measurements were performed using a dilution refrigerator at the M15 beamline at TRIUMF. Multiple LaRhGe₃ crystals were mounted on an Ag plate using GE varnish and placed on the sample holder. Careful canceling of the remnant field was performed using a Si semiconductor reference prior to the zero-field experiment following the method of Ref. [72]. The transverse-field experiment was performed by applying a magnetic field along the plate direction of the sample in spin-rotated mode. Muon analysis was performed in MUSRFIT [73].

D. Raman Measurements

Raman scattering measurements were performed using a Horiba Jobin-Yvon LabRAM monochromator,

equipped with 1800 grooves/mm grating and a Peltier cooled CCD camera. The 632.817 nm line of a He-Ne laser was used as the light source, and the spot diameter is about 10 μ m on the sample using a 50x microscopic objective for both focusing and collection of light. The spectral resolution is about 1 cm⁻¹ in this study. A Semrock RazorEdge filter was used to block the elastically scattered laser light, where the cutoff energy is 79 cm⁻¹. For measured performed at non-ambient temperatures, we used a Cryovac Micro continuous helium flow cryostat, where the sample is thermally anchored to the copper cold-finger and sits in a vacuum environment better than 1×10^{-6} mbar. Measurements were taken at temperatures ranging between 5 to 300 K with 1 K accuracy.

LaRhGe₃ has five atoms in the primitive cell, leading to a total of three acoustic and 12 optical phonon bands. With visible light, Raman scattering only probes a small portion of the Brillouin zone near $q = 0$, where the symmetries of the 12 optical phonons can be denoted by the irreducible representations of the C_{4v} point group: $3A_1 + B_1 + 4E$ [65]. The samples was mounted on the cryostat with the as-grown (101) surface normal to the optical axis. At room temperature, spectra were obtained with the incident and scattered light polarized in the following combinations in order to identify the symmetries of the studied excitations: $(E_i, E_s) = (x, x)$ couples to phonons with A_1, B_1 and E symmetries, $(E_i, E_s) = (x, y)$ couples only to phonons with the E symmetry. E_i and E_s are the polarizations of the incident and scattered light, respectively. x and y corresponds to $[10\bar{1}]$ and $[010]$ crystal axes, respectively. The analyzing polarizer is removed in temperature dependent experiments to collect data from all phonons in the same cooling cycle.

E. DFT Calculations

Electronic structure calculations were performed within the framework of density functional theory (DFT) as implemented in the VASP package [74–76]. The generalized gradient approximation with the PBE parameterization for the exchange-correlation functional [77, 78] was used. The plane-wave-basis set has been cut off at $E_{\text{cutoff}} = 287.6$ eV and the charge density was converged on a grid of 1792 irreducible k points. The tetragonal crystal structure ($I4mm$, space group no. 107, $a = 4.432$ Å, and $c = 10.101$ Å) was used [26], and structural relaxation resulted in $a = 4.437$ Å, and $c = 10.281$ Å. The phonon modes were computed in a $2 \times 2 \times 1$ conventional supercell using the phonopy package[79, 80].

V. DATA AVAILABILITY

The data that support the findings of this study are available from the corresponding authors upon reasonable request.

VI. AUTHOR INFORMATION

A. Contributions

Single crystals were grown by S.S., M.O., and A.M.H. Heat capacity and electrical transport measurements and analysis were performed by M.O. Room temperature Raman measurements were performed by H.H.K. and M.O., and low temperature Raman measurements were performed by A.S. and B.K. Analysis of Raman data were performed by H.H.K. Thermal transport and Seebeck measurements were performed by K.P. and H.T. DFT calculations were performed by N.H. and A.P.S. Muon measurements and analysis were performed by M.V.T.S., Y.C., M.O., and K.K. Manuscript was written by M.O., H.H.K., N.H., D.A.B., and A.M.H., with feedback from other co-authors.

VII. ETHICS DECLARATIONS

A. Competing interests

the Authors declare no Competing Financial or Non-Financial Interests

ACKNOWLEDGMENTS

This research was undertaken thanks in part to funding from the Max Planck-UBC-UTokyo Centre for Quantum Materials and the Canada First Research Excellence Fund, Quantum Materials and Future Technologies Program. This work was also supported by the Natural Sciences and Engineering Research Council of Canada (NSERC), the CIFAR Azrieli Global Scholars program, and the Sloan Research Fellowships program. We thank TRIUMF staff for their technical support during muon experiment. We thank K. Behnia, E. Benckiser, M. Minola, S. Dierker, and M. Sigrist for valuable discussion.

-
- [1] KS Novoselov, AK Geim, SV Morozov, D Jiang, MI Katsnelson, IV Grigorieva, SV Dubonos, and AA Firsov, “Two-dimensional gas of massless Dirac fermions in graphene,” *Nature* **438**, 197–200 (2005).
- [2] Andre K Geim and Konstantin S Novoselov, “The rise of graphene,” *Nat. Mater.* **6**, 183–191 (2007).
- [3] AA Burkov, “Topological semimetals,” *Nat. Mater.* **15**, 1145–1148 (2016).
- [4] Binghai Yan and Claudia Felser, “Topological materials: Weyl semimetals,” *Annu. Rev. Condens. Matter Phys.* **8**, 337–354 (2017).
- [5] NP Armitage, EJ Mele, and Ashvin Vishwanath, “Weyl and Dirac semimetals in three-dimensional solids,” *Rev. Mod. Phys.* **90**, 015001 (2018).
- [6] Mazhar N Ali, Jun Xiong, Steven Flynn, Jing Tao, Quinn D Gibson, Leslie M Schoop, Tian Liang, Neel Haldolaarachchige, Max Hirschberger, Nai Phuan Ong, *et al.*, “Large, non-saturating magnetoresistance in WTe₂,” *Nature* **514**, 205–208 (2014).
- [7] Chandra Shekhar, Ajaya K Nayak, Yan Sun, Marcus Schmidt, Michael Nicklas, Inge Leermakers, Uli Zeitler, Yurii Skourski, Jochen Wosnitza, Zhongkai Liu, *et al.*, “Extremely large magnetoresistance and ultrahigh mobility in the topological Weyl semimetal candidate NbP,” *Nat. Phys.* **11**, 645–649 (2015).
- [8] Nitesh Kumar, Yan Sun, Nan Xu, Kaustuv Manna, Mengyu Yao, Vicky Süß, Inge Leermakers, Olga Young, Tobias Förster, Marcus Schmidt, *et al.*, “Extremely high magnetoresistance and conductivity in the type-II Weyl semimetals WP₂ and MoP₂,” *Nat. Commun.* **8**, 1642 (2017).
- [9] M-Y Yao, Nan Xu, QS Wu, Gabriel Autès, Nitesh Kumar, Vladimir N Strocov, Nicholas C Plumb, Milan Radovic, Oleg V Yazyev, Claudia Felser, *et al.*, “Observation of weyl nodes in robust type-II Weyl semimetal WP₂,” *Phys. Rev. Lett.* **122**, 176402 (2019).
- [10] Gavin B. Osterhoudt, Yaxian Wang, Christina A. C. Garcia, Vincent M. Plisson, Johannes Gooth, Claudia Felser, Prineha Narang, and Kenneth S. Burch, “Evidence for dominant phonon-electron scattering in Weyl semimetal WP₂,” *Phys. Rev. X* **11**, 011017 (2021).
- [11] Yun Wu, Lin-Lin Wang, Eundeok Mun, Duane D Johnson, Daixiang Mou, Lunan Huang, Yongbin Lee, Serguei L Bud’ko, Paul C Canfield, and Adam Kaminski, “Dirac node arcs in PtSn₄,” *Nat. Phys.* **12**, 667–671 (2016).
- [12] Chenguang Fu, Satya N Guin, Thomas Scaffidi, Yan Sun, Rana Saha, Sarah J Watzman, Abhay K Srivastava, Guowei Li, Walter Schnelle, Stuart SP Parkin, *et al.*, “Largely suppressed magneto-thermal conductivity and enhanced magneto-thermoelectric properties in PtSn₄,” *Research* (2020).
- [13] Hung-Yu Yang, Xiaohan Yao, Vincent Plisson, Shirin Mozaffari, Jan P Scheifers, Aikaterini Flessa Savvidou, Eun Sang Choi, Gregory T McCandless, Mathieu F Padlewski, Carsten Putzke, Philip J. W. Moll, Jula Y. Chan, Luis Balicas, Kenneth S. Burch, and Fazel Tafti, “Evidence of a coupled electron-phonon liquid in NbGe₂,” *Nat. Commun.* **12**, 5292 (2021).
- [14] Eve Emmanouilidou, Sougata Mardanya, Jie Xing, PV Sreenivasa Reddy, Amit Agarwal, Tay-Rong Chang, and Ni Ni, “Fermiology and type-I superconductivity in

- the chiral superconductor NbGe₂ with Kramers-Weyl fermions,” *Phys. Rev. B* **102**, 235144 (2020).
- [15] E. Bauer, G. Hilscher, H. Michor, Ch. Paul, E. W. Scheidt, A. Griбанov, Yu. Seropegin, H. Noël, M. Sigrist, and P. Rogl, “Heavy fermion superconductivity and magnetic order in noncentrosymmetric CePt₃Si,” *Phys. Rev. Lett.* **92**, 027003 (2004).
- [16] E. Bauer and M. Sigrist, *Non-Centrosymmetric Superconductors: Introduction and Overview* (Berlin: Springer, 2012).
- [17] M Smidman, M B Salamon, H Q Yuan, and D F Agterberg, “Superconductivity and spin-orbit coupling in non-centrosymmetric materials: a review,” *Rep. Prog. Phys.* **80**, 036501 (2017).
- [18] Sungkit Yip, “Noncentrosymmetric superconductors,” *Annu. Rev. Condens. Matter Phys.* **5**, 15–33 (2014).
- [19] Andreas P Schnyder and Philip M R Brydon, “Topological surface states in nodal superconductors,” *J. Phys. Condens. Matter* **27**, 243201 (2015).
- [20] N Kimura, K Ito, K Saitoh, Y Umeda, H Aoki, and T Terashima, “Pressure-induced superconductivity in noncentrosymmetric heavy-fermion CeRhSi₃,” *Phys. Rev. Lett.* **95**, 247004 (2005).
- [21] Ichiro Sugitani, Yusuke Okuda, Hiroaki Shishido, Tsutomu Yamada, Arumugam Thamizhavel, Etsuji Yamamoto, Tatsuma D Matsuda, Yoshinori Haga, Tetsuya Takeuchi, Rikio Settai, *et al.*, “Pressure-induced heavy-fermion superconductivity in antiferromagnet CeIrSi₃ without inversion symmetry,” *J. Phys. Soc. Jpn.* **75**, 043703–043703 (2006).
- [22] Yusuke Okuda, Yuichiro Miyauchi, Yuki Ida, Yuuji Takeda, Chie Tonohiro, Yasuhiro Ouchi, Tsutomu Yamada, Nguyen Duc Dung, Tatsuma D. Matsuda, Yoshinori Haga, *et al.*, “Magnetic and superconducting properties of LaIrSi₃ and CeIrSi₃ with the non-centrosymmetric crystal structure,” *J. Phys. Soc. Jpn.* **76**, 044708 (2007).
- [23] Noriaki Kimura, Yuji Muro, and Haruyoshi Aoki, “Normal and superconducting properties of noncentrosymmetric heavy fermion CeRhSi₃,” *J. Phys. Soc. Jpn.* **76**, 051010–051010 (2007).
- [24] Rikio Settai, Tetsuya Takeuchi, and Yoshichika Ōnuki, “Recent advances in Ce-based heavy-fermion superconductivity and Fermi surface properties,” *J. Phys. Soc. Jpn.* **76**, 051003 (2007).
- [25] Marie-aude Méasson, Hiroshi Muranaka, Tomoya Kawai, Yuuki Ota, Kiyohiro Sugiyama, Masayuki Hagiwara, Koichi Kindo, Tetsuya Takeuchi, Katsuya Shimizu, Fuminori Honda, *et al.*, “Magnetic properties of RCoGe₃ (R: Ce, Pr, and Nd) and strong anisotropy of the upper critical field in non-centrosymmetric compound CeCoGe₃,” *J. Phys. Soc. Jpn.* **78**, 124713 (2009).
- [26] Tomoya Kawai, Hiroshi Muranaka, Toyoaki Endo, Nguyen Duc Dung, Yusuke Doi, Shugo Ikeda, Tatsuma D Matsuda, Yoshinori Haga, Hisatomo Harima, Rikio Settai, and Yoshichika Onuki, “Split Fermi surface properties of LaTGe₃ (T: transition metal) and PrCoGe₃ with the non-centrosymmetric crystal structure,” *J. Phys. Soc. Jpn.* **77**, 064717–064717 (2008).
- [27] G Eguchi, DC Peets, M Kriener, Y Maeno, E Nishibori, Y Kumazawa, K Banno, S Maki, and H Sawa, “Crystallographic and superconducting properties of the fully gapped noncentrosymmetric 5d-electron superconductors CaMSi₃ (M = Ir, Pt),” *Phys. Rev. B* **83**, 024512 (2011).
- [28] Masaaki Isobe, Hiroyuki Yoshida, Koji Kimoto, Masao Arai, and Eiji Takayama-Muromachi, “SrAuSi₃: A noncentrosymmetric superconductor,” *Chemistry of Materials* **26**, 2155–2165 (2014).
- [29] Paul C Canfield and Z Fisk, “Growth of single crystals from metallic fluxes,” *Philos. Mag. B* **65**, 1117–1123 (1992).
- [30] G Venturini, M Méot-Meyer, B Malaman, and B Roques, “De nouvelles séries de germaniures, isotopes de Yb₃Rh₄Sn₁₃ et BaNiSn₃, dans les systèmes ternaires TR–T–Ge où TR est un élément des terres rares et T ≡ Co, Rh, Ir, Ru, Os,” *J. Less-Common Met.* **113**, 197–204 (1985).
- [31] Moritz M Hirschmann, Andreas Leonhardt, Berkay Kilic, Douglas H Fabini, and Andreas P Schnyder, “Symmetry-enforced band crossings in tetragonal materials: Dirac and Weyl degeneracies on points, lines, and planes,” *Phys. Rev. Mater.* **5**, 054202 (2021).
- [32] Hongming Weng, Yunye Liang, Qiunan Xu, Rui Yu, Zhong Fang, Xi Dai, and Yoshiyuki Kawazoe, “Topological node-line semimetal in three-dimensional graphene networks,” *Phys. Rev. B* **92**, 045108 (2015).
- [33] Y.-H. Chan, Ching-Kai Chiu, M. Y. Chou, and Andreas P. Schnyder, “Ca₃P₂ and other topological semimetals with line nodes and drumhead surface states,” *Phys. Rev. B* **93**, 205132 (2016).
- [34] C. K. Chiu, Y. H. Chan, and A. P. Schnyder, “Quantized berry phase and surface states under reflection symmetry or space-time inversion symmetry,” *arXiv preprint arXiv:1810.04094* (2018).
- [35] Pengzi Liu, James R Williams, and Judy J Cha, “Topological nanomaterials,” *Nat. Rev. Mater.* **4**, 479–496 (2019).
- [36] Jifa Tian, Ireneusz Miotkowski, Seokmin Hong, and Yong P Chen, “Electrical injection and detection of spin-polarized currents in topological insulator Bi₂Te₂Se,” *Sci. Rep.* **5**, 14293 (2015).
- [37] Jifa Tian, Seokmin Hong, Ireneusz Miotkowski, Supriyo Datta, and Yong P Chen, “Observation of current-induced, long-lived persistent spin polarization in a topological insulator: A rechargeable spin battery,” *Sci. Adv.* **3**, e1602531 (2017).
- [38] Peng Li, Weikang Wu, Yan Wen, Chenhui Zhang, Junwei Zhang, Senfu Zhang, Zhiming Yu, Shengyuan A Yang, Aurelien Manchon, and Xi-xiang Zhang, “Spin-momentum locking and spin-orbit torques in magnetic nano-heterojunctions composed of Weyl semimetal WTe₂,” *Nat. Commun.* **9**, 3990 (2018).
- [39] Jimin Kim, Seung Su Baik, Sae Hee Ryu, Yeongsup Sohn, Soohyung Park, Byeong-Gyu Park, Jonathan Denlinger, Yeonjin Yi, Hyoung Joon Choi, and Keun Su Kim, “Observation of tunable band gap and anisotropic Dirac semimetal state in black phosphorus,” *Science* **349**, 723–726 (2015).
- [40] Rex Lundgren, Pontus Laurell, and Gregory A Fiete, “Thermoelectric properties of Weyl and Dirac semimetals,” *Phys. Rev. B* **90**, 165115 (2014).
- [41] Qinsheng Wang, Cai-Zhen Li, Shaofeng Ge, Jin-Guang Li, Wei Lu, Jiawei Lai, Xuefeng Liu, Junchao Ma, Da-Peng Yu, Zhi-Min Liao, *et al.*, “Ultrafast broadband photodetectors based on three-dimensional Dirac semimetal Cd₃As₂,” *Nano letters* **17**, 834–841 (2017).

- [42] Chunyu Guo, Lunhui Hu, Carsten Putzke, Jonas Diaz, Xiangwei Huang, Kaustuv Manna, Feng-Ren Fan, Chandra Shekhar, Yan Sun, Claudia Felser, Chaoping Liu, B. Andrei Bernevig, and Philip J. W. Moll, “Quasi-symmetry-protected topology in a semi-metal,” *Nature Physics* **18**, 813–818 (2022).
- [43] Chao Shang, Owen Ganter, Niclas Heinsdorf, and Stephen M. Winter, “irf₄: From tetrahedral compass model to topological semimetal,” *Phys. Rev. B* **107**, 125111 (2023).
- [44] V. Gurarie, “Single-particle green’s functions and interacting topological insulators,” *Phys. Rev. B* **83**, 085426 (2011).
- [45] Zhong Wang and Shou-Cheng Zhang, “Simplified topological invariants for interacting insulators,” *Phys. Rev. X* **2**, 031008 (2012).
- [46] Xue-Yang Song and Andreas P. Schnyder, “Interaction effects on the classification of crystalline topological insulators and superconductors,” *Phys. Rev. B* **95**, 195108 (2017).
- [47] Mikel Iraola, Niclas Heinsdorf, Apoorv Tiwari, Dominik Lessnich, Thomas Mertz, Francesco Ferrari, Mark H. Fischer, Stephen M. Winter, Frank Pollmann, Titus Neupert, Roser Valentí, and Maia G. Vergniory, “Towards a topological quantum chemistry description of correlated systems: The case of the hubbard diamond chain,” *Phys. Rev. B* **104**, 195125 (2021).
- [48] Rajesh Chaunsali, Haitao Xu, Jinkyu Yang, Panayotis G. Kevrekidis, and Georgios Theocharis, “Stability of topological edge states under strong nonlinear effects,” *Phys. Rev. B* **103**, 024106 (2021).
- [49] Yuxuan Wang and Rahul M. Nandkishore, “Topological surface superconductivity in doped weyl loop materials,” *Phys. Rev. B* **95**, 060506 (2017).
- [50] Alfred Brian Pippard, *Magnetoresistance in metals*, Vol. 2 (Cambridge university press, 1989).
- [51] Yi-Yan Wang, Qiao-He Yu, Peng-Jie Guo, Kai Liu, and Tian-Long Xia, “Resistivity plateau and extremely large magnetoresistance in NbAs₂ and TaAs₂,” *Phys. Rev. B* **94**, 041103 (2016).
- [52] Aifeng Wang, D Graf, Yu Liu, Qianheng Du, Jiabao Zheng, Hechang Lei, and C Petrovic, “Large magnetoresistance in the type-II Weyl semimetal WP₂,” *Phys. Rev. B* **96**, 121107 (2017).
- [53] J Bannies, E Razzoli, M Michiardi, H-H Kung, IS Elfmov, M Yao, A Fedorov, J Fink, C Jozwiak, A Bostwick, *et al.*, “Extremely large magnetoresistance from electron-hole compensation in the nodal-loop semimetal ZrP₂,” *Phys. Rev. B* **103**, 155144 (2021).
- [54] Qi Wang, Qiangwei Yin, and Hechang Lei, “Magnetotransport properties of compensated semimetal hfb2 with high-density light carriers,” *J. Condens. Matter Phys.* **32**, 015601 (2019).
- [55] Niraj Bhattarai, Andrew W Forbes, Christopher Gassen, Raghad SH Saqat, Ian L Pegg, and John Philip, “Experimental study of transport properties of weyl semimetal laalge thin films grown by molecular beam epitaxy,” *J. Vac. Sci. Technol. A* **39** (2021).
- [56] E Svanidze and E Morosan, “Type-i superconductivity in ScGa₃ and LuGa₃ single crystals,” *Phys. Rev. B* **85**, 174514 (2012).
- [57] Liang L Zhao, Stefan Lausberg, Hyunsoo Kim, Makariy A Tanatar, Manuel Brando, Ruslan Prozorov, and E Morosan, “Type-i superconductivity in YbSb₂ single crystals,” *Phys. Rev. B* **85**, 214526 (2012).
- [58] Shanshan Sun, Kai Liu, and Hechang Lei, “Type-i superconductivity in KBi₂ single crystals,” *J. Condens. Matter Phys.* **28**, 085701 (2016).
- [59] VK Anand, AD Hillier, DT Adroja, AM Strydom, H Michor, KA McEwen, and BD Rainford, “Specific heat and μ SR study on the noncentrosymmetric superconductor LaRhSi₃,” *Phys. Rev. B* **83**, 064522 (2011).
- [60] GW Hull, JH Wernick, TH Geballe, JV Waszczak, and JE Bernardini, “Superconductivity in the ternary intermetallics YbPd₂Ge₂, LaPd₂Ge₂, and LaPt₂Ge₂,” *Phys. Rev. B* **24**, 6715 (1981).
- [61] TTM Palstra, G Lu, AA Menovsky, GJ Nieuwenhuys, PH Kes, and JA Mydosh, “Superconductivity in the ternary rare-earth (Y, La, and Lu) compounds RPd₂Si₂ and RRh₂Si₂,” *Phys. Rev. B* **34**, 4566 (1986).
- [62] Shingo Yonezawa and Yoshiteru Maeno, “Type-I superconductivity of the layered silver oxide Ag₅Pb₂O₆,” *Phys. Rev. B* **72**, 180504 (2005).
- [63] Carolina A Marques, Matthew James Neat, Chi Ming Yim, Matthew David Watson, Luke Charles Rhodes, Christoph Heil, KS Pervakov, VA Vlasenko, VM Pudalov, AV Muratov, *et al.*, “Electronic structure and superconductivity of the non-centrosymmetric Sn₄As₃,” *New J. Phys.* **22**, 063049 (2020).
- [64] Clifford W Hicks, Alexandra S Gibbs, Andrew P Mackenzie, Hiroshi Takatsu, Yoshiteru Maeno, and Edward A Yelland, “Quantum oscillations and high carrier mobility in the delafossite PdCoO₂,” *Physical Review Letters* **109**, 116401 (2012).
- [65] E. Kroumova, M.I. Aroyo, J.M. Perez-Mato, A. Kirov, C. Capillas, S. Ivantchev, and H. Wondratschek, “Bilbao crystallographic server : Useful databases and tools for phase-transition studies,” *Phase Transitions* **76**, 155–170 (2003).
- [66] William Hayes and Rodney Loudon, *Scattering of light by crystals* (Wiley, 1978).
- [67] Nicola Bonini, Michele Lazzeri, Nicola Marzari, and Francesco Mauri, “Phonon anharmonicities in graphite and graphene,” *Phys. Rev. Lett.* **99**, 176802 (2007).
- [68] Philip B. Allen and Richard Silbergliitt, “Some effects of phonon dynamics on electron lifetime, mass renormalization, and superconducting transition temperature,” *Phys. Rev. B* **9**, 4733–4741 (1974).
- [69] H-N Liu, X Cong, M-L Lin, and P-H Tan, “The intrinsic temperature-dependent Raman spectra of graphite in the temperature range from 4K to 1000K,” *Carbon* **152**, 451–458 (2019).
- [70] José Menéndez and Manuel Cardona, “Temperature dependence of the first-order Raman scattering by phonons in Si, Ge, and α - Sn: Anharmonic effects,” *Phys. Rev. B* **29**, 2051–2059 (1984).
- [71] Mai Ye, H.-H. Kung, Priscila F. S. Rosa, Eric D. Bauer, Zachary Fisk, and Girsh Blumberg, “Raman spectroscopy of *f*-electron metals: An example of CeB₆,” *Phys. Rev. Mater.* **3**, 065003 (2019).
- [72] GD Morris and RH Heffner, “A method of achieving accurate zero-field conditions using muonium,” *Physica B: Condensed Matter* **326**, 252–254 (2003).
- [73] A Suter and BM Wojek, “MUSRFIT: a free platform-independent framework for μ SR data analysis,” *Physics Procedia* **30**, 69–73 (2012).
- [74] G. Kresse and J. Hafner, “Ab initio molecular dynamics for liquid metals,” *Phys. Rev. B* **47**, 558–561 (1993).

- [75] Georg Kresse and Jürgen Furthmüller, “Efficiency of ab-initio total energy calculations for metals and semiconductors using a plane-wave basis set,” *Comput. Mater. Sci.* **6**, 15–50 (1996).
- [76] G. Kresse and J. Furthmüller, “Efficient iterative schemes for ab initio total-energy calculations using a plane-wave basis set,” *Phys. Rev. B* **54**, 11169–11186 (1996).
- [77] John P Perdew, Kieron Burke, and Yue Wang, “Generalized gradient approximation for the exchange-correlation hole of a many-electron system,” *Phys. Rev. B* **54**, 16533 (1996).
- [78] John P. Perdew, Kieron Burke, and Matthias Ernzerhof, “Generalized gradient approximation made simple,” *Phys. Rev. Lett.* **77**, 3865–3868 (1996).
- [79] A Togo and I Tanaka, “First principles phonon calculations in materials science,” *Scr. Mater.* **108**, 1–5 (2015).
- [80] Atsushi Togo, “First-principles phonon calculations with Phonopy and Phono3py,” *J. Phys. Soc. Jpn.* **92**, 012001 (2023).
- [81] WL McMillan, “Transition temperature of strongly-coupled superconductors,” *Phys. Rev.* **167**, 331 (1968).
- [82] YJ Uemura, “Condensation, excitation, pairing, and superfluid density in high- t_c superconductors: the magnetic resonance mode as a roton analogue and a possible spin-mediated pairing,” *J. Condens. Matter Phys.* **16**, S4515 (2004).
- [83] Ernst Bauer, RT Khan, Herwig Michor, Esmail Royanian, A Grytsiv, N Melnychenko-Koblyuk, P Rogl, D Reith, R Podloucky, E-W Scheidt, *et al.*, “BaPtSi₃: A noncentrosymmetric BCS-like superconductor,” *Phys. Rev. B* **80**, 064504 (2009).
- [84] F Kneidinger, L Salamakha, E Bauer, I Zeiringer, P Rogl, C Blaas-Schenner, D Reith, and R Podloucky, “Superconductivity in noncentrosymmetric BaAl₄ derived structures,” *Phys. Rev. B* **90**, 024504 (2014).
- [85] Jiro Kitagawa, Yuji Muro, Naoya Takeda, and Masayasu Ishikawa, “Low-temperature magnetic properties of several compounds in Ce–Pd–x ($x = \text{Si, Ge and Al}$) ternary systems,” *J. Phys. Soc. Jpn.* **66**, 2163–2174 (1997).
- [86] M Smidman, AD Hillier, DT Adroja, MR Lees, V Kn Anand, Ravi P Singh, RI Smith, DM Paul, and G Balakrishnan, “Investigations of the superconducting states of noncentrosymmetric LaPdSi₃ and LaPtSi₃,” *Phys. Rev. B* **89**, 094509 (2014).
- [87] V Kn Anand, D Britz, A Bhattacharyya, DT Adroja, AD Hillier, AM Strydom, W Kockelmann, BD Rainford, and Kn A McEwen, “Physical properties of noncentrosymmetric superconductor LaIrSi₃: A μ SR study,” *Phys. Rev. B* **90**, 014513 (2014).
- [88] Ravi P Singh, AD Hillier, D Chowdhury, JAT Barker, D McK Paul, MR Lees, and G Balakrishnan, “Probing the superconducting ground state of the noncentrosymmetric superconductors CaT₂Si₃ ($T = \text{Ir, Pt}$) using muon-spin relaxation and rotation,” *Phys. Rev. B* **90**, 104504 (2014).
- [89] Kn Miliyanchuk, Friedrich Kneidinger, C Blaas-Schenner, D Reith, R Podloucky, P Rogl, T Khan, L Salamakha, G Hilscher, H Michor, *et al.*, “Platinum metal silicides and germanides: superconductivity in non-centrosymmetric intermetallics,” in *J. Phys. Conf. Ser.*, Vol. 273 (IOP Publishing, 2011) p. 012078.
- [90] PP Poole, HA Farach, RJ Creswick, and R Prozorov, “Superconductivity,” (2007).
- [91] JP Carbotte, “Properties of boson-exchange superconductors,” *Rev. Mod. Phys.* **62**, 1027 (1990).
- [92] Gerald E Peabody and R Meservey, “Magnetic flux penetration into superconducting thin films,” *Phys. Rev. B* **6**, 2579 (1972).
- [93] Devashibhai T Adroja, Franziska KK Kirschner, Franz Lang, Michael Smidman, Adrian D Hillier, Zhi-Cheng Wang, Guang-Han Cao, Gavin BG Stenning, and Stephen J Blundell, “Multigap superconductivity in RbCa₂Fe₄As₄F₂ investigated using μ SR measurements,” *J. Phys. Soc. Japan* **87**, 124705 (2018).
- [94] Mohammed A Albedah, Farshad Nejadstari, Zbigniew M Stadnik, Zhi-Cheng Wang, Cao Wang, and Guang-Han Cao, “Absence of the stripe antiferromagnetic order in the new 30 k superconductor ThFeAsN,” *J. Alloys Compd.* **695**, 1128–1136 (2017).
- [95] A Bhattacharyya, DT Adroja, M Smidman, and VK Anand, “A brief review on μ SR studies of unconventional Fe- and Cr-based superconductors,” *Sci. China: Phys. Mech. Astron.* **61**, 1–22 (2018).
- [96] JE Sonier, SA Sabok-Sayr, FD Callaghan, CV Kaiser, V Pacradouni, JH Brewer, SL Stubbs, WN Hardy, DA Bonn, Ruixing Liang, and W. A. Atkinson, “Hole-doping dependence of the magnetic penetration depth and vortex core size in YBa₂Cu₃O_y: Evidence for stripe correlations near 1/8 hole doping,” *Phys. Rev. B* **76**, 134518 (2007).
- [97] YJ Uemura, “Muon spin relaxation studies on high- t_c , organic, heavy-fermion, and Chevrel phase superconductors,” *Phys. B: Condens. Matter* **169**, 99–106 (1991).
- [98] Evgeny F Talantsev and Jeffery L Tallon, “Universal self-field critical current for thin-film superconductors,” *Nat. Commun.* **6**, 7820 (2015).
- [99] YJ Uemura, GM Luke, BJ Sternlieb, JH Brewer, JF Carolan, WN Hardy, R Kadono, JR Kempton, RF Kiefl, SR Kreitzman, *et al.*, “Universal correlations between t_c and n_s/m^* (carrier density over effective mass) in high- t_c cuprate superconductors,” *Phys. Rev. Lett.* **62**, 2317 (1989).
- [100] Xiao Lin, Zengwei Zhu, Benoît Fauqué, and Kamran Behnia, “Fermi surface of the most dilute superconductor,” *Phys. Rev. X* **3**, 021002 (2013).

Supplemental Materials:
Discovery of Superconductivity and Electron-Phonon Drag in
the Non-Centrosymmetric Semimetal LaRhGe₃

Supporting details on the crystal structure of LaRhGe₃

TABLE S1. LaRhGe₃ crystals structure refinement fit results.

Parameter	Value
Chemical Formula	LaRhGe ₃
Formula weight	459.73
Temperature (K)	300
Crystal System	Tetragonal
Space Group	<i>I4mm</i>
<i>a</i> , (Å)	4.4187(2)
<i>c</i> , (Å)	10.0494(5)
Volume (Å ³)	196.21(6)
Z	2
ρ_{calc} (g/cm ³)	7.781
Radiation	Cu _k α_1 = 1.5406 Å
R_{Bragg}	1.544

TABLE S2. Refined atomic positions of LaRhGe₃.

Atom	<i>x</i>	<i>y</i>	<i>z</i>
La	0.0	0.0	0.0
Rh	0.0	0.0	0.65762
Ge1	0.0	0.0	0.42106
Ge2	0.0	0.5	0.25990

Supporting details on the normal state transport of LaRhGe₃

TABLE S3. Comparing de Haas-van Alphen (dHvA) oscillations Frequency in our LaRhGe₃ samples with Literature [S26].

Branch	F ($\times 10^7$ Oe)	F _{literature} ($\times 10^7$ Oe) [S26]
ϵ (1st)	3.09	3.06
ϵ (2nd)	3.06	3.04
θ (1st)	0.43	0.44
θ (2nd)	0.38	0.38
η (1st)	0.082	0.08
η (2nd)	0.065	0.06

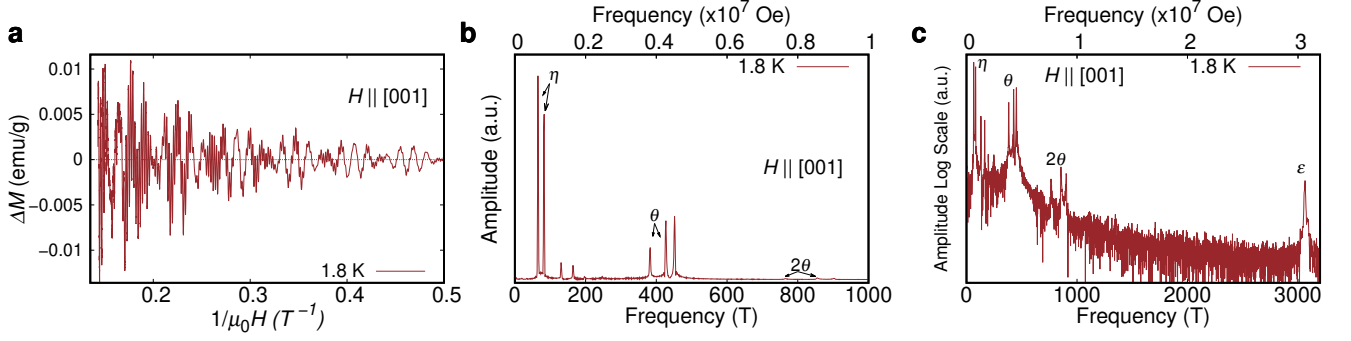


FIG. S1. (a) Oscillatory component ΔM corresponding to the de Haas-van Alphen (dHvA) oscillations in LaRhGe₃ measured at 1.8 K. (b) and (c) Fast Fourier Transform spectrum of the dHvA oscillations in (a).

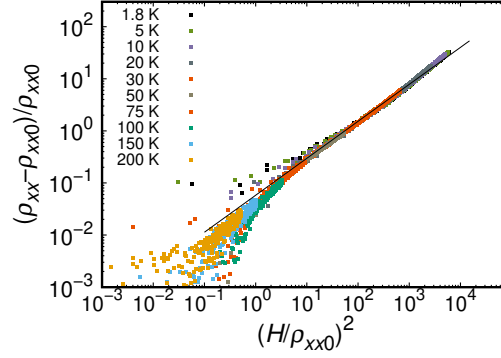


FIG. S2. Kohler scaling analysis of MR data shown in main text (Fig. 4). Any change of slope related to the electron phonon drag in the current data is unclear.

Supporting details on the superconductivity of LaRhGe₃

To further characterize the superconductivity of LaRhGe₃, we next turn to modelling its specific heat. Above $T_c = 0.39(1)$ K the C_P data are well described by

$$C_p = \gamma_n T + \beta T^3 \quad (\text{S1})$$

where fitting the data yields the Sommerfeld coefficient $\gamma_n = 4.92(4)$ mJ mol⁻¹ K⁻² and $\beta = 0.25(1)$ mJ mol⁻¹ K⁻⁴. The phonon contribution is represented by the cubic term βT^3 and the Debye temperature Θ_D is then calculated according to

$$\Theta_D = \left(\frac{12\pi^4}{5\beta} nR \right)^{1/3} \quad (\text{S2})$$

where n , the number of atoms per formula unit, is 5 and R is the gas constant 8.314 J mol⁻¹ K⁻¹, giving $\Theta_D = 341(10)$ K. Next, taking Θ_D and T_c , we calculate the superconducting parameter λ_{ep} using the inverted McMillan [S81] equation

$$\lambda_{ep} = \frac{1.04 + \mu^* \ln \left(\frac{\Theta_D}{1.45 T_c} \right)}{(1 - 0.62 \mu^*) \ln \left(\frac{\Theta_D}{1.45 T_c} \right) - 1.04} \quad (\text{S3})$$

where $\mu^* = 0.10$ and $T_c = 0.39(1)$ K. We find $\lambda_{ep} = 0.34(2)$ for LaRhGe₃, suggesting it is a weak coupling superconductor. Using λ_{ep} , γ , and the Boltzmann constant k_B , we calculate the electronic density of states (DOS) at the Fermi energy $N(E_F)$ with the equation

$$N(E_F) = \frac{3\gamma}{\pi^2 k_B^2 (1 + \lambda_{ep})} \quad (\text{S4})$$

TABLE S4. Superconductivity in LaRhGe₃ compared with other superconductors in *I4mm* space group.

Compound	T_c (K)	γ_n (mJ mol ⁻¹ K ⁻²)	$B_{c2}(0)$ (T)	Reference
Ba(Pt,Pd)Si ₃	2.3–2.8	4.9–5.7	0.05–0.10	[S83, S84]
La(Rh,Pt Pd,Ir)Si ₃	0.7–2.7	4.4–6	Type I/0.053	[S22, S59, S85–S87]
Ca(Pt,Ir)Si ₃	2.3–3.6	4.0–5.8	0.15–0.27	[S27, S88]
Sr(Ni,Pd,Pt)Si ₃	1.0–3.0	3.9–5.3	0.039–0.174	[S84]
Sr(Pd,Pt)Ge ₃	1.0–1.5	4.0–5.0	0.03–0.05	[S84, S89]
LaRhGe ₃	0.39(1)	4.92(4)	Type I/0.0021(1)	This work

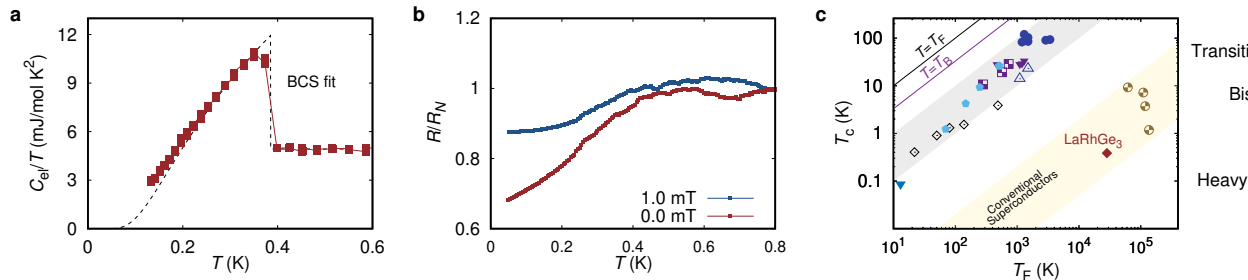


FIG. S3. Type-I BCS nature of the superconducting state in LaRhGe₃. (a) Superconducting transition of LaRhGe₃ in the electronic part of the specific heat C_{el}/T as a function of T in 0 T. The dashed black line is a fit for a T_c of 0.39(1) K for weak-coupling BCS behavior. (b) Temperature dependence of longitudinal resistivity ρ_{xx} below 0.6 K measured in different magnetic fields, where the data are normalized by the 2.0 K data ($\rho_{xx,2\text{ K}} \sim 1 \mu\Omega\text{cm}$) measured in 0 mT. (c) Zero field μSR spectra collected at 539 mK and 20 mK, with fit using Kubo-Toyabe function for the data. No significant change is seen between the data above and below T_c . Inset shows the resulting relaxation rate σ . (d) Uemura plot showing the superconducting transition temperature (T_c) vs the Fermi temperature (T_F) for various superconductors [S82, S90–S100], where LaRhGe₃ falls within the region of conventional superconductors. $T = T_B$ line in purple represents the Bose-Einstein condensation temperature of an ideal three-dimensional boson gas, and $T = T_F$ line is shown in black.

$N(E_F)$ was estimated to be 1.56 states eV^{-1} per formula unit of LaRhGe₃. From our DFT calculations we find the DOS at the Fermi energy $N(E_F)^{calc}$ of 3.24 states eV^{-1} per formula unit, and we evaluate the effective mass based on specific heat to be $m^*/m_e = N(E_F)/N(E_F)^{calc} = 0.54$. This reduced effective mass compared with the free electron mass is consistent with LaRhGe₃ being a semimetal, and the value of $m^*/m_e = 0.54$ falls within the cyclotron effective masses, $m^*/m_e \sim 0.23\text{--}1.04$, reported previously by Kawai *et al.* [S26].

The magnitude of the specific heat jump $\Delta C/C_{en} \sim 1.43$, C_{en} being the electronic specific heat in the normal state, is consistent with that expected for a BCS model in the weak-coupling limit. The BCS model, shown in black in Fig. S3(a), fits the data well just below T_c , but some deviations appears at lower temperatures. With the current C_P we cannot conclude whether the gap structure of LaRhGe₃ is an isotropic *s*-wave gap or whether the gap structure has some nodes, and this will be the subject of future experiments going to lower temperatures.

In Table S4, we compare the T_c , γ_n , and $B_c(0)$ values for various superconductors in the *I4mm* space group, including LaRhGe₃ and LaRhSi₃. Despite the comparable γ_n values for all of these materials, we have varying superconducting T_c and critical fields. Whether this difference is due to details of electronic band structure or atomic size effects is unclear at the moment.

We evaluate the Fermi temperature T_F for a 3D system via the relation $T_F = (\hbar^2/2)(3\pi^2)^{2/3}n^{2/3}/k_B m^*$ [S82], where n is the density of quasiparticles per unit volume. We use the low temperature carrier density from our Hall measurements and the effective mass estimated from specific heat to obtain $T_F = 28340\text{ K}$ and $T_c/T_F = 1.36 \times 10^{-5}$, which places LaRhGe₃ in a region with other conventional superconductors (Fig. S3(c)). This further confirms that the ternary compound LaRhGe₃ can be described in the bulk as a BCS superconductor in the weak-coupling limit.

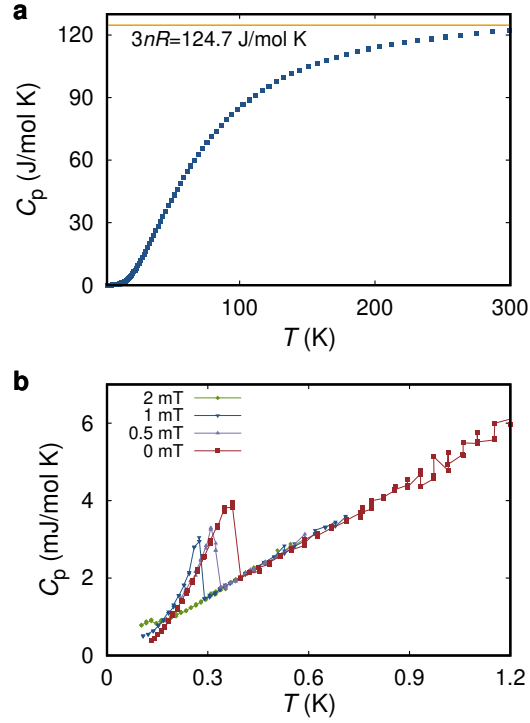


FIG. S4. (a) Temperature dependence of C_P measured between 2-300 K, which shows that the high temperature region approaches the Dulong-Petit limit. (b) Temperature dependence of C_P measured in different applied magnetic fields, showing the superconducting transition, $T_c 0.39(1)$ K in zero-field, that gets suppressed with applied field. Fit to the data above T_c to the form γ and β taking into account the electronic and the phononic contributions. The phononic contribution was subtracted to obtain the C_{el} in the main text.

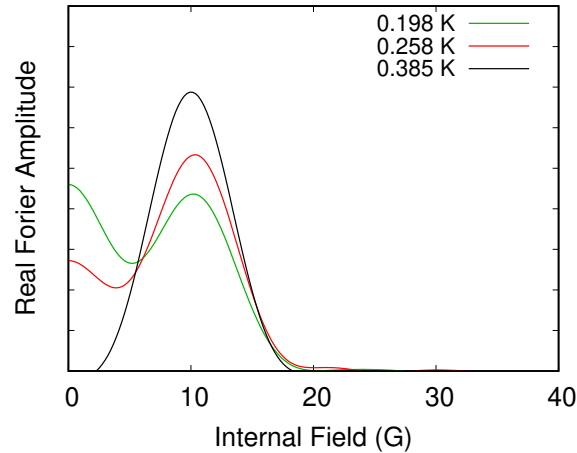


FIG. S5. The Fourier transform of μ SR asymmetry for different temperatures in an applied field of 10 G (1 mT). A shift in the amplitude from the peak around 10 G to zero field is observed as we enter the superconducting state. No significant increase in the field of the oscillating component can be resolved from this data collected in low magnetic field.

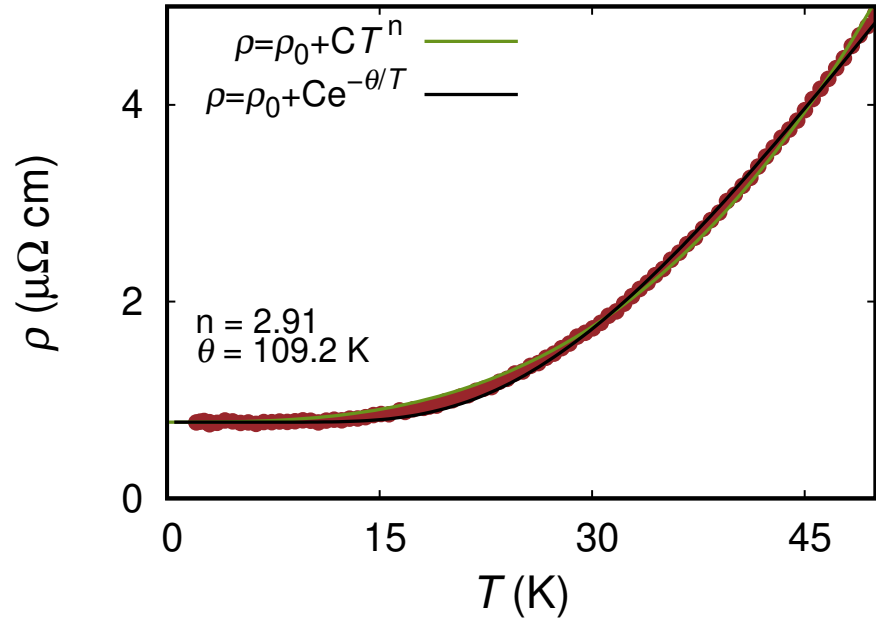


FIG. S6. Resistivity as a function of temperature measured along ab -plane of LaRhGe_3 in zero-field, where data is fitted to exponential form of a phonon-drag model, $\rho = \rho_0 + Ce^{-T_0/T}$ and power law fit $\rho = \rho_0 + CT^n$ below 50 K.

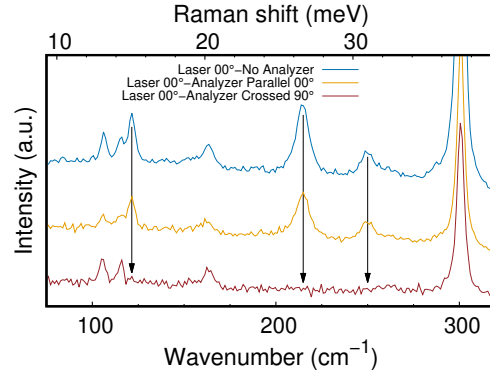
Supporting details on the Raman measurements of LaRhGe₃

FIG. S7. Raman spectra collected with fixed linearly polarized laser, and polarization analyzer at different orientations. The blue curve shows data without the analyzer (mixed parallel and perpendicular); orange curve is the analyzer polarization parallel to the laser (xx geometry); red curve is the analyzer 90° rotated with respect to laser polarization (xy geometry). Three phonon modes that are strongly suppressed were highlighted with arrows, demonstrating that these are A_1 modes of LaRhGe₃.

TABLE S5. Calculated energies and symmetries of the phonon modes for LaRhGe₃ and comparison with the fitting parameters of Eq. 5 based on our Raman spectra in Fig. S8. All units are in cm⁻¹. The errors represent one standard deviation of the least-squared fit.

DFT	$\omega(10\text{ K})$	ω_0	ω_1	ω_{3p}	γ_0	γ_{3p}	γ_{ep}	ω_a	
$E^{(1)}$	98.1	107.0(1)	107.3(1)	$\omega_0/2$	0.18(8)	1.8(4)	0.27(6)	2.3(7)	47(4)
$E^{(2)}$	108.6	116.3(1)	116.6(1)	$\omega_0/2$	0.14(19)	1.6(5)	0.36(8)	2.0(9)	39(19)
$A_1^{(1)}$	112.8	124.9(1)	125.2(1)	$\omega_0/2$	0.60(2)	0.9(8)	0.59(14)	9.9(15)	61(1)
$B_1^{(1)}$	159.1	141.6(6)	142.6(4)	$\omega_0/2$	0.50(60)	0(17)	1.0(30)	24(29)	71(5)
$E^{(3)}$	162.0	166.2(2)	167.2(1)	$\omega_0/2$	0.86(2)	3(10)	0.7(18)	2.1(77)	-14(645)
$A_1^{(2)}$	207.9	219.9(0)	221.1(1)	$\omega_0/2$	1.85(5)	8.2(1)	0.22(3)	-	-
$A_1^{(3)}$	240.8	255.2(0)	256.6(4)	52(6)	1.4(4)	5.1(1)	0.84(4)	-	-
$E^{(4)}$	252.7	267.1(3)	268.8(15)	61(22)	1.6(15)	1.4(9)	2.4(3)	-	-

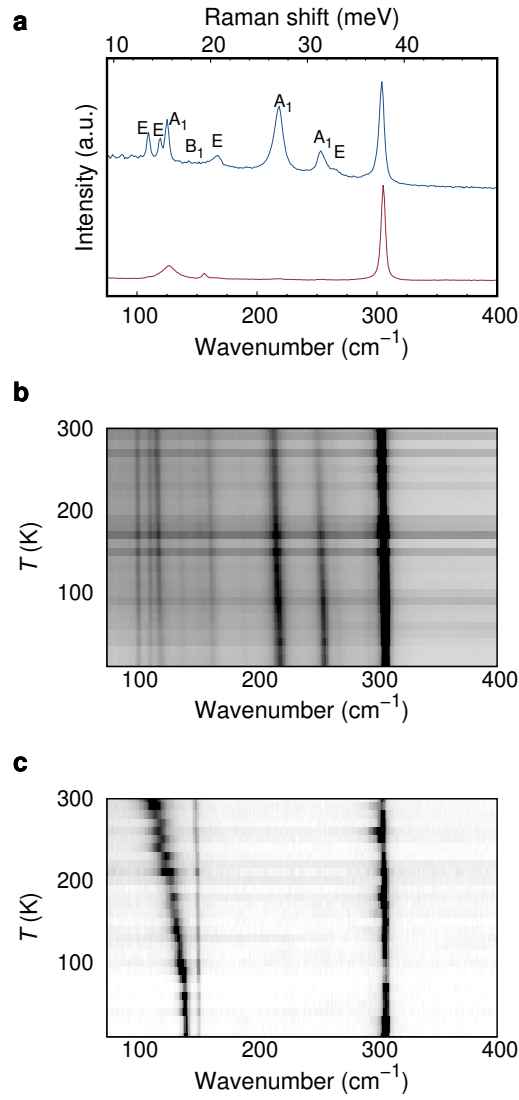


FIG. S8. (a) Raman spectra of LaRhGe_3 measured along different directions of the crystal at room temperature. (b) Black and white map of Raman scattering intensity plotted as a function of temperature and Raman shift measured from the (101) surface of LaRhGe_3 crystal. Unless otherwise specified, all of the Raman data in this work were taken from this sample. (c) Black and white map of Raman scattering intensity measured from the same sample as panel (b), but from a different spot. Since these data were not reproduced by other crystals that we measured, this spot is likely a crystallite with different orientation and possibly even different stoichiometry as the host crystal. However, we highlight the mode at 144 cm^{-1} at 10 K where the energy softens drastically with increasing temperature, to 120 cm^{-1} at 300 K. Such large temperature dependence is highly unusual and is difficult to reconcile with the moderate anharmonicity found in LaRhGe_3 . The energy of this mode is in the vicinity of the the $A_1^{(1)}$ mode that shows strong electron-phonon coupling, raising the possibility of electron-phonon induced self-energy effect. However, more study is required on this crystallite before any conclusion can be drawn. In this paper, our discussion is focused on data in panel (b) which is reproduced across samples.

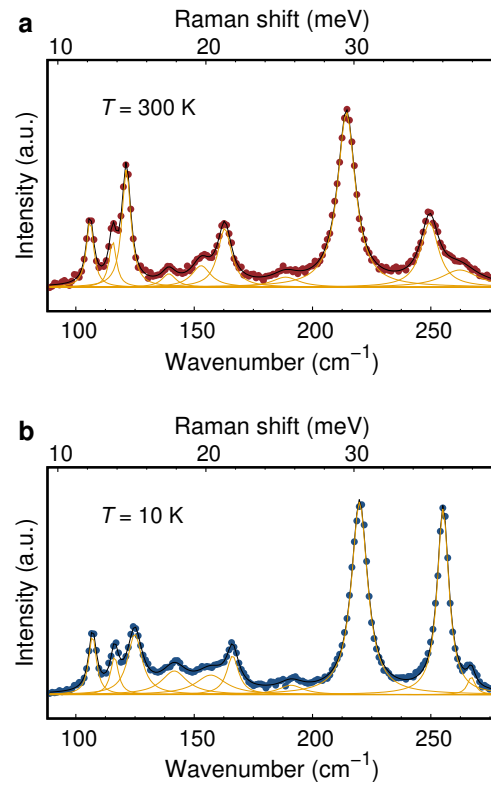


FIG. S9. Raman spectra of LaRhGe_3 measured at 300 K (a) and 10 K (b), sliced from Fig. S8(b) to showcase the extraction of phonon energy and width through fitting. Measured data shown as points and fitted curves for each phonon mode shown individually in yellow and total fit in black.